Bioactive Materials 39 (2024) 406–426

Contents lists available at ScienceDirect

Bioactive Materials

journal homepage: www.keaipublishing.com/en/journals/bioactive-materials

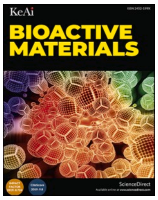

Engineered SPIONs functionalized with endothelin a receptor antagonist ameliorate liver fibrosis by inhibiting hepatic stellate cell activation

Marit ten Hove [a], Andreas Smyris [a], Richell Booijink [a], Lydia Wachsmuth [b], Uwe Hansen [c], Lejla Alic [d], Cornelius Faber [b], Carsten Höltke [b], Ruchi Bansal [a,*]

[a] *Personalized Diagnostics and Therapeutics, Department of Bioengineering Technologies, Technical Medical Centre, Faculty of Science and Technology, University of Twente, Enschede, the Netherlands*
[b] *Clinic of Radiology, University Hospital Muenster, Muenster, Germany*
[c] *Institute for Musculoskeletal Medicine, University Hospital Muenster, Muenster, Germany*
[d] *Department of Magnetic Detection and Imaging, Technical Medical Centre, Faculty of Science and Technology, University of Twente, Enschede, the Netherlands*

ARTICLE INFO

Keywords:
Endothelin A receptor
SPIONs
Hepatic stellate cells
Liver fibrosis

ABSTRACT

Endothelin-1/endothelin A receptor (ET-1/ETAR) pathway plays an important role in the progression of liver fibrosis by activating hepatic stellate cells (HSCs) - a key cell type involved in the pathogenesis of liver fibrosis. Inactivating HSCs by blocking the ET-1/ETAR pathway using a selective ETAR antagonist (ERA) represents a promising therapeutic approach for liver fibrosis. Unfortunately, small-molecule ERAs possess limited clinical potential due to poor bioavailability, short half-life, and rapid renal clearance. To improve the clinical applicability, we conjugated ERA to superparamagnetic iron-oxide nanoparticles (SPIONs) and investigated the therapeutic efficacy of ERA and ERA-SPIONs in vitro and in vivo and analyzed liver uptake by in vivo and ex vivo magnetic resonance imaging (MRI), HSCs-specific localization, and ET-1/ETAR-pathway antagonism in vivo. In murine and human liver fibrosis/cirrhosis, we observed overexpression of ET-1 and ETAR that correlated with HSC activation, and HSC-specific localization of ETAR. ERA and successfully synthesized ERA-SPIONs demonstrated significant attenuation in TGFβ-induced HSC activation, ECM production, migration, and contractility. In an acute CCl_4-induced liver fibrosis mouse model, ERA-SPIONs exhibited higher liver uptake, HSC-specific localization, and ET-1/ETAR pathway antagonism. This resulted in significantly reduced liver-to-body weight ratio, plasma ALT levels, and α-SMA and collagen-I expression, indicating attenuation of liver fibrosis. In conclusion, our study demonstrates that the delivery of ERA using SPIONs enhances the therapeutic efficacy of ERA in vivo. This approach holds promise as a theranostic strategy for the MRI-based diagnosis and treatment of liver fibrosis.

1. Introduction

Liver injuries due to metabolic disorders, excessive alcohol consumption, and/or hepatitis viral infections can lead to the development of liver fibrosis [1–3]. Hepatic stellate cells (HSCs) play a pivotal role in the progression of liver fibrosis [4–8]. Upon activation, HSCs proliferate and transdifferentiate into myofibroblasts, and secrete excessive amounts of extracellular matrix (ECM) components causing structural alterations in the liver, and gradual loss of liver function [4–7]. Fibrosis, at an early stage, can be reversed when the underlying cause is eliminated, if left untreated, fibrosis progresses to cirrhosis, end-stage liver failure, or hepatocellular carcinoma (HCC, primary liver cancer). Liver fibrosis is a leading and growing cause of mortality worldwide, yet currently, there are no FDA-approved anti-fibrotic therapies available [9,10].

One of the pathways involved in fibrosis is the endothelin-1 (ET-1) pathway. ET-1, a 21-amino acid peptide produced by endothelial cells, is a potent vasoconstrictor with proliferative, pro-fibrotic, and pro-inflammatory properties, and is involved in the pathophysiology of several diseases including fibrosis and cancer [11–19]. ET-1 mediates its effects by interacting with two G-coupled protein receptors, endothelin A receptor (ETAR) and endothelin B receptor (ETBR), which are widely

---

Peer review under responsibility of KeAi Communications Co., Ltd.

* Corresponding author. Carre 4419, Drienerlolaan 5, 7522NB, Enschede, the Netherlands.
E-mail address: r.bansal@utwente.nl (R. Bansal).

https://doi.org/10.1016/j.bioactmat.2024.05.034
Received 16 November 2023; Received in revised form 16 May 2024; Accepted 17 May 2024

expressed in different tissues. ET-1 exhibits a 100-fold higher affinity for ETAR compared to ETBR, and its biological effects are highly diverse depending on the receptor expression [14,15]. In the liver, ETAR is specifically localized on HSCs while ETBR is present on various liver cell types [13–15,20,21]. ETAR (and sometimes ETBR) activation triggers the recruitment of one or more G-protein families and scaffold proteins e.g., β-arrestins, that stimulate diverse downstream signal-transduction pathways including extracellular-signal-regulated kinase (ERK) signaling, resulting in a range of pleiotropic responses [22].

During liver diseases, circulating levels of ET-1 are increased, which positively correlates with disease severity [20,21,23–26]. Transforming growth factor-beta (TGFβ), the key regulator of fibrosis, induces ET-1 production by regulating the post-transcriptional processing of ET-1 [23,27]. Subsequently, ET-1 promotes HSC activation via ETAR [28]. Conversely, activated HSCs upregulate the expression and affinity of ET-1 and ETAR, resulting in an autocrine and paracrine loop of HSC activation mediated by ET-1 [26,29]. ET-1 also induces HSC contraction, chemotaxis, proliferation, and synthesis of collagen-I, –III, and fibronectin, while downregulating the activity of matrix metalloproteinase-1 (MMP-1) [27]. Collectively, the ET-1/ETAR pathway contributes to the progression of liver fibrosis via HSC activation suggesting antagonism of the ET-1/ETAR pathway could inhibit HSC activation and consequently liver fibrosis.

Previously, Rockey et al. showed that Bosentan, an ETAR/ETBR antagonist, reduced HSC activation and fibrosis in carbon tetrachloride (CCl_4) and bile-duct ligation (BDL) models of liver fibrosis [27]. Furthermore, Thirunavukkarasu et al. reported that treatment with TAK-044, another ETAR/ETBR antagonist, reduced collagen synthesis and expression of tissue inhibitors of matrix metalloproteinases (TIMPs)-1, 2, and TGFβ, attenuating liver fibrosis in CCl_4/phenobarbital model [30]. Feng et al. investigated selective ETAR and ETBR antagonists and found that ETAR antagonism reduced portal pressure whereas ETBR antagonism increased portal pressure. However, chronic administration of both antagonists inhibited CCl_4-induced liver fibrosis [31]. Lastly, Cho et al. showed that LU-135252, a selective and oral ETAR antagonist, decreased collagen, TIMP-1, and TIMP-2 expression in the BDL model [32]. Altogether, these results indicate that antagonism of endothelin receptors is a promising therapeutic approach to target hepatic fibrosis. Notably, selective ETAR antagonism is preferred over ETBR or dual receptor antagonism since ETBR functions as a clearance receptor for ET-1 [29,33]. ETBR antagonism may compromise ET-1 clearance resulting in increased ET-1 levels [25,33,34], suggesting selective ETAR antagonism is preferable for targeting the ET-1 pathway during liver fibrosis [32].

The clinical application of ETAR antagonists is unfortunately hindered due to their poor bioavailability, short half-life, and rapid renal clearance [34]. These limitations necessitate the administration of multiple doses, increasing the risk of adverse effects. Alternative strategies are hence required to improve the stability (and half-life), bioavailability, and (hepatic) selective organ-cellular uptake of ETAR antagonists. The use of nanoparticles as a delivery strategy holds great promise here [35–37]. Among nanoparticles, superparamagnetic iron-oxide nanoparticles (SPIONs) present an attractive option due to their biocompatibility, colloidal stability, and large surface area for functionalization [38–41]. Dextran-polyethylene glycol (PEG)-coated SPIONs possess functional groups that allow for easy functionalization with therapeutic agents. Besides, dextran-PEG coating improves biocompatibility and blood circulation [38–41]. Furthermore, SPIONs possess magnetic properties enabling their detection using magnetic resonance imaging (MRI), making them suitable for theranostic (therapeutic and diagnostic) applications. We have previously shown the potential of SPIONs for the delivery of biologicals (relaxin and fibroblast growth factor-2) to inhibit fibrosis and fibrotic-rich tumor stroma in CCl_4-induced liver fibrosis model and pancreatic tumor models respectively [42–45]. Engineered SPIONs have been previously utilized for biomedical applications, for example, SPIONs mediated mitochondrial transfer from human mesenchymal stem cells selectively to diseased cells, which mitigated pulmonary fibrosis in vivo [46]; bone-targeted SPIONs positively regulated bone metabolism and attenuated post-menopausal osteoporosis [47]; and TRPV1 antibodies conjugated to SPIONs (in combination with alternating magnetic field stimulation) effectively impeded macrophagic inflammation and chondrocyte ferroptosis in osteoarthritis [48]. Moreover, SPIONs have been introduced for MRI-based tracking of immune cells e.g., for immunotherapy monitoring [49,50]. These examples emphasize the versatile utilization of engineered SPIONs.

In this study, we investigated the potential of HSC-specific delivery of CH948, a selective ETAR antagonist (ERA), using SPIONs to inhibit HSC activation and attenuate liver fibrosis. CH948 is based on PD-156707, a potent and highly selective ETAR antagonist [51,52], where one methoxy group is replaced by an amino group via a PEG-spacer to enable coupling reactions [53]. Previous studies showed that CH948-fluorescent probes can be used for in vivo imaging of ETAR in mouse models of cancer or myocardial infarction [53–56]. Here, we first examined the expression of ET-1 and ETAR in liver fibrosis and then investigated the therapeutic effects of CH948 (ERA) on TGFβ-activated HSCs in vitro. Next, we conjugated ERA to the surface of dextran-PEG-coated SPIONs, using carbodiimide chemistry, to synthesize ERA-SPIONs, followed by extensive characterization of the nanoparticles. We then evaluated the therapeutic effects of ERA-SPIONs compared to ERA and SPIONs on TGFβ-activated HSCs in vitro. Thereafter, ERA and ERA-SPIONs were fluorescently labeled to monitor their biodistribution in an acute CCl_4-induced liver fibrosis mouse model using in vivo imaging and liver uptake was confirmed using MRI. We also investigated the HSC-specific localization of ERA-SPIONs and ETAR antagonism in vivo. Finally, we assessed the therapeutic effects of ERA-SPIONs versus ERA in the liver fibrosis mouse model. Altogether, we have developed a versatile HSC-targeted nano-theranostic enabling (multimodal) diagnostic imaging and treatment of liver fibrosis.

2. Materials and methods

2.1. Gene expression analysis

2.1.1. Transcriptomic profiles of human liver tissue

To analyze the endothelin gene expression, a human liver tissue transcriptome dataset (GSE14323) was selected from the Gene Expression Omnibus (GEO) database (National Center for Biotechnology Information, US). GSE14323 comprises the transcriptomic profiles from 19 normal healthy individuals and 41 cirrhotic patients [57]. GEO2R was used to assess the expression of endothelin-1, endothelin A receptor, and collagen-I in normal and cirrhotic human livers, and correlation analysis was performed to correlate collagen-I expression with endothelin A receptor.

2.1.2. Single cell transcriptomic profiles of human and mouse livers

To analyze the endothelin A receptor gene expression at single cell level, the human and mouse Liver Cell Atlas databases [58] were used. Gene expression for '*EDNRA*' was used to obtain UMAP plots of the single cell expression in the $CD45^-$ liver cell types.

2.2. Synthesis of ERA-SPIONs

The selective endothelin A receptor antagonist CH948 (referred to as ERA) used in this study is based on α-[2-(4-Methoxyphenyl)-2-oxo-1-[(3,4,5-trimethoxyphenyl)methyl]ethylidene]-1,3-benzodioxole-5-acetic acid sodium salt (PD-156707) [51,52,59]. In CH948 one methoxy group is modified with an amino group using a PEG-spacer enabling coupling reactions at this site [54]. The preparation, characterization, and use of CH948 have been previously described elsewhere by Höltke et al. [54]. The conjugation of ERA (CH948) to dextran-coated PEG-COOH functionalized superparamagnetic iron oxide nanoparticles, (SPIONs, nanomag®-D-spio, 20 nm core size, Micromod Partikeltechnologie, GmbH, Rostock, Germany) was chemically performed with carbodiimide chemistry as described previously [42–45]. 100 μL of SPIONs (5 mg/mL) were activated with 10 μmol 1-ethyl-3-(3-dimethylaminopropyl) carbodiimide hydrochloride (EDC, Sigma, St. Louis, MO, USA) and 35 μmol N-hydroxysuccinimide (NHS, Sigma) prepared in 125 μL of 2(-N-morpholino) ethanesulfonic acid (MES, Sigma) buffer (pH 6.3). After 45 min of reaction with gentle shaking at room temperature, SPIONs were washed thrice with 300 μL of phosphate-buffered saline (PBS) and purified using 30 kDa Amicon™ Ultra Centrifugal Filters (Merck Millipore, Darmstadt, Germany) by centrifugation at 5000×*g*. Eventually, the activated SPIONs were reacted with 0.1 mM ERA--PEG-NH_2 overnight at 4 °C with gentle shaking. Samples were then purified using 30 kDa Amicon™ Ultra Centrifugal Filters by three washing steps with 300 μL PBS each. Wash solutions were collected for analysis by HPLC to determine the coupling efficiency of ERA to SPIONs by calculating starting ERA concentrations minus ERA in wash solutions. SPIONs were reacted with 10 μg glycine (Sigma) for 30 min at RT to deactivate the remaining activated COOH groups. Similarly, a batch (glycine-SPIONs) without ERA modification was synthesized as a control. SPIONs were again purified using 30 kDa Amicon™ Ultra Centrifugal Filters, resuspended in PBS, and stored at 4 °C.

For biodistribution studies, 100 μL SPIONs (5 mg/mL) were reacted with 10 μL of 1 mM Cy5.5-NH_2 (Lumiprobe, Hannover, Germany) with and without 2 μL of 5 mM ERA-PEG-NH_2 overnight at 4 °C with gentle shaking to obtain SPIONs-Cy5.5 and ERA-SPIONs-Cy5.5 followed by extensive washing steps with PBS to remove free unconjugated ERA-PEG-NH_2 and Cy5.5. Samples were stored at 4 °C protected from light.

2.3. Characterization of ERA-SPIONs

2.3.1. Size and zeta potential measurements

The hydrodynamic size and zeta potential of the (unmodified) SPIONs, glycine-SPIONs, ERA-SPIONs, and respective Cy5.5 constructs were measured using a Nano ZS Zetasizer (Malvern Instruments Ltd., Malvern, UK). To evaluate the hydrodynamic size and the polydispersity index (PdI), 5 μL of SPIONs, Glycine-SPIONs, ERA-SPIONs, SPIONs-Cy5.5 or ERA-SPIONs-Cy5.5 were diluted in 1 mL MilliQ or PBS and loaded in a 1 mL polystyrene cuvette. To evaluate the zeta potential, 5 μL of SPIONs, Glycine-SPIONs, ERA-SPIONs, SPIONs-Cy5.5, or ERA-SPIONs-Cy5.5 were diluted in 1 mL 10 mM KCl and loaded (Malvern Instruments, UK). To evaluate the stability, the SPIONs and ERA-SPIONs were stored at 4 °C for 4 months after which the hydrodynamic size and zeta potential were measured using a Nano ZS Zetasizer (Malvern Instruments Ltd).

To access the stability of nanoparticles in different physiological media, we measured the hydrodynamic size of the unmodified SPIONs and ERA-SPIONs. 5 μL of SPIONs or ERA-SPIONs were diluted in 1 mL MilliQ, PBS, Dulbecco's Modified Eagle's Medium (DMEM) or RPMI 1640 medium (RPMI). DMEM, high glucose, with GlutaMAX (Thermo Fisher) was supplemented with 1 % Penicillin/Streptomycin (Capricorn Scientific). RMPI with L-Glutamine (Capricorn Scientific) was supplemented with 1 % Penicillin/Streptomycin. Samples were also prepared containing 10 % fetal bovine serum (FBS, Lonza, Verviers, Belgium) and additionally MilliQ samples containing 50 % FBS. 5 min after supplementation of the nanoparticles to the media the hydrodynamic diameter of all individual peaks within a sample, together with corresponding area percentages, and the polydispersity index was measured in a 1 mL polystyrene cuvette at 37 °C. Medium was also measured without SPIONs or ERA-SPIONs as controls.

2.3.2. Transmission and scanning electron microscopy

For Transmission Electron Microscopy (TEM), small aliquots of the nanoparticles were absorbed to Formvar/carbon-coated copper grids for 10 min. After washing with distilled water, grids with absorbed material were negatively stained with 2 % (w/v) uranyl acetate for 15 min. Transmission electron micrographs were taken at 60 kV with a Phillips EM-410 electron microscope using imaging plates (Ditabis, Pforzheim, Germany).

For High-Resolution Scanning Electron Microscopy (HRSEM), samples were prepared by drop-casting of each suspension onto a clean SiO_2 substrate. Within 2 h, the liquid has completely evaporated, leaving a coffee-stain ring of nanoparticles. No further sample conditioning was necessary for subsequent SEM imaging. HRSEM measurements were performed using a Merlin Field Emission SEM (FE-SEM) from Zeiss. The microscope is equipped with an on-axis in-lens secondary electron detector as well as a high efficiency off-axis secondary electron detector. The in-lens detector is a high efficiency detector for SE1 and SE2 and owes its superb imaging results to the geometric position in the beam path and the combination with the electrostatic/electromagnetic lens. This detector is in particular powerful at low voltages provided a small working distance can be reached.

For High-Resolution TEM and Energy Dispersive X-Ray spectroscopy (EDX), the samples were prepared by drop-casting on a honey-carbon grid. TEM measurements were performed with a Spectra 300 from Thermo Fisher Scientific with a high tension of 300 kV. Images of the particles were made in a parallel-beam TEM mode, as well as in a convergent-beam scanning mode (STEM). In scanning mode, the images were done with a High Angle Annular Dark Field (HAADF) detector. EDX was performed in STEM configuration with a beam current of about 60 pA and a convergence angle of 28 mrad.

2.3.3. MALDI-TOF mass spectrometry

SPIONs and ERA-SPIONs were analyzed with matrix-assisted laser desorption/ionization time of flight mass spectrometry (MALDI-TOF MS) using the MALDI-TOF/TOF smartfleX (Bruker Daltonics GmbH & Co. KG, Bremen, Germany). Samples were prepared using the matrix of α-Cyano-4-hydroxycinnamic acid (HCCA) which was dissolved to saturation in a mixture of 30 % acetonitrile and 70 % water with trifluoroacetic acid (0.1 % v/v) (TA30). SPIONs were diluted 1:20 with TA30, of which 0.5 μL was spotted onto a stainless-steel target and was air-dried before insertion into the vacuum.

2.3.4. Iron content measurement

A colorimetric Prussian blue assay was used to assess the iron concentration of SPIONs based on the method described by Ozdemir et al. [60]. In the assay, a calibration curve was plotted by preparing serially diluted SPIONs solution (iron concentrations ranging from 0.3 to 1.2 mg/mL) in PBS. Samples were also prepared by serially diluting in PBS (1:1 and 1:2). All samples (5 μL), including standards, together with 75 μL 1.2 N hydrochloric acid solution (Sigma) was digested at 65 °C for 1 h for the conversion of iron from nanoparticle form to ionic form. 80 μL 1.2 N hydrochloric acid solution and 20 μL 4 % w/v potassium ferrocyanide solution (Sigma) was then added to the samples. Three independent repeats of each sample were prepared for the measurement, and 5 μL of PBS was used as blank. Samples were incubated for 25 min at room temperature, and the absorbance was measured at 690 nm using the i-control microplate reader (Tecan, Männedorf, Switzerland). The iron concentration of the samples was determined using a standard curve prepared using the known iron concentrations of SPIONs.

2.3.5. High-performance liquid chromatography measurements

High-performance liquid chromatography (HPLC) was used to indirectly quantify the conjugation efficiency of ERA to the SPIONs by measuring the unconjugated CH948 (ERA) molecules before and after conjugation. HPLC was performed on a Reversed Phase-HPLC (RP-HPLC) Shimadzu Prominence system (Shimadzu Deutschland GmbH, Duisburg, Germany) using a Aeris Peptide XB-C18 HPLC column (Phenomenex, Torrance, CA) and a mobile phase containing water (H_2O) and acetonitrile (ACN) with 0.1 % trifluoroacetic acid (TFA) using a gradient from 80:20 (H_2O:ACN) to 30:70 (H_2O:ACN) at a flowrate of 1.5 mL/min. The protocol for HPLC is as follows: 1 min 80:20 (H_2O:ACN); 19 min

80:20–30:70 (H_2O:ACN) gradient; 8 min 30:70–80:20 (H_2O:ACN) gradient; 1 min 80:20 (H_2O:ACN). CH948 (ERA) was detected at 254 nm and eluted at 12.6 min. The concentration of ERA (CH948) was determined by analyzing peak areas using calibration curves and ERA coupling efficiency (%) was calculated by analyzing the starting ERA concentration minus ERA concentration found in the wash solutions.

2.3.6. FTIR analysis of SPIONs

To confirm the modification of SPIONs with ERA, Fourier transformation infrared (FTIR) spectroscopy was performed on SPIONs, Glycine-SPIONs, and ERA-SPIONs. These measurements were conducted using a Shimadzu IRSpirit FTIR-spectrophotometer in the 4000-600 cm^{-1} spectral range. Data were collected and the water background was eliminated.

2.3.7. VSM measurements

The magnetic properties of ERA-SPIONs and SPIONs were analyzed using the Quantum Design Physical Property Measurement System (PPMS, Quantum Design Inc., San Diego, CA, USA) at the University of Twente at room temperature. For VSM measurements, 15 μL of PBS (used for the sample holder control), SPIONs, or ERA-SPIONs was added in a small glass container. The iron content of SPIONs and ERA-SPIONs corresponded to 36 μg of iron per sample. Magnetic moment versus magnetic field was calculated for ERA-SPIONs and SPIONs and visualized in an $M - H$ curve.

2.3.8. Relaxation measurements

Longitudinal (T1) and transverse (T2) relaxation times were obtained using 0.5 T MRI (FOV: 15 × 15 × 15 mm) at 37 °C using SPIONs and ERA-SPIONs phantoms, where SPIONs or ERA-SPIONs were diluted in PBS to concentrations of 0.2, 0.1, 0.05, and 0.025 mM Fe. Data for all phantoms were acquired in five-fold. T1 was determined using an inversion recovery sequence with $T_R = 5 * T1$ estimated and 12 logarithmically increasing inversion times starting from 3 ms to T_R. A monoexponentially fitted signal was used to assess the T1 value. T2 was determined using a multi-spin echo sequence with $T_R = 5 * T1$ estimated and 32 echoes with starting TE from 0.5 ms to TR. A monoexponentially fitted signal was used to assess the T2 value. For all five individual acquisitions per phantom, the $R1 = 1/T1$ and $R2 = 1/T2$ (1/s) were plotted against the contrast agent concentration (mM Fe) and were fitted with a simple linear regression. The slopes of these lines represent the corresponding longitudinal (r_1) and transverse (r_2) relaxivities in L/mmol-s.

Additionally, longitudinal (T1) and transversal (T2) relaxation times of ERA SPIO and free SPIO phantoms with concentrations of 0.2, 0.1, 0.05, and 0.025 mM Fe diluted in PBS were measured at 9.4 T at 23 °C (three dilution series each). T1 was determined using a RARE sequence with TRs of 5500, 3000, 1500, 800, 400, 200 ms, TE 7 ms, FOV 2.5 cm, 128 matrices, 1 slice, 1,5 mm slice thickness. T2 was determined using an MSME sequence with TR 7500 ms and 64 echo times, min TE 7.4 ms, echo spacing 7.4 ms, and the same geometry parameters. We used monoexponential fitting as implemented in PV6.01. The values of $R1 = 1/T1$ and $R2 = 1/T2$ in s were plotted versus contrast agent concentration in mM Fe and were fitted with a simple linear regression. The slopes represent the respective longitudinal (r_1) and transversal (r_2) relaxivities in L/mmol-s.

2.3.9. Fluorescent intensity measurements

Serial dilutions of SPIONs-Cy5.5, ERA-SPIONs-Cy5.5, ERA-Cy5.5, and Cy5.5 were prepared in PBS (1, 1:1, 1:2 dilutions), and 5 μL of each sample was spotted on a Petri dish. Near-infrared fluorescence was measured using the Pearl Trilogy Small Animal Imaging System (LI-COR Biosciences, Lincoln, NE) at 255 μm resolution using the 700-channel laser source (excitation: 685 nm; emission: 720 nm).

2.4. In vitro effect of ERA and ERA-SPIONS on TGFβ-activated HSCs

2.4.1. LX-2 cells

LX-2 cells, an immortalized cell line of human HSCs, provided by Prof. Scott Friedman (Mount Sinai Hospital, New York, NY, USA) were cultured in DMEM-Glutamax supplemented with 10 % FBS, 50 U/mL penicillin and 50 μg/mL streptomycin at 37°C in a humidified atmosphere (37 °C with 5 % CO_2).

2.4.2. Binding studies

Cells were seeded in 24-well plates ($2*10^4$ cells/well) and cultured for 24 h. Cells were starved overnight with serum-free medium and subsequently incubated with TGFβ (5 ng/mL, Roche, Mannheim, Germany) for 24 h. For binding studies, cells (±TGFβ) were incubated with ERA, SPIONs, or ERA-SPIONs (equivalent to 100 nM ERA) for 2 h at room temperature. Cells were washed thrice with PBS and were fixed with 4 % formalin. Iron oxide was detected using the Prussian Blue staining kit (Sigma) containing potassium ferrocyanide and hydrochloric acid in a 1:1 ratio for 30 min at room temperature. Images were captured using a Nikon E400 microscope (Nikon, Tokyo, Japan).

2.4.3. Metabolic activity

To examine the effect of ERA and ERA-SPIONs on the metabolic activity of the LX-2 cells, Alamar blue assays were performed. Cells were seeded in 96-well plates ($5*10^3$ cells/well) and cultured for 24 h. Cells were serum-starved for 24 h and incubated with different concentrations of ERA (50 nM, 100 nM), 100 nM SPIONs, or ERA-SPIONs (equivalent to 100 nM ERA), together with TGFβ (5 ng/mL) for 24 h. Metabolic activity assay was performed using Alamar Blue reagent (Invitrogen) as per manufacturer's instructions. The cells were incubated with Alamar Blue reagent for 4 h and fluorescent signals were measured using a VIKTOR™ plate reader (Perkin Elmer, Waltham, MA). The results were represented as % cell viability normalized to TGFβ-activated control cells (at 100 %).

2.4.4. Gene and protein expression

The effect of ERA and ERA-SPIONs on gene expression was investigated in LX-2 cells using quantitative real-time PCR. The effect of ERA and ERA-SPIONs on protein expression was investigated in LX-2 cells using western blot analysis and immunohistochemistry. Cells were seeded in 12-well plates ($1*10^5$ cells/well) for quantitative real-time PCR, in 12-well plates ($8*10^4$ cells/well) for western blot, or in 24-well plates ($5*10^4$ cells/well) for immunohistochemistry and subsequently cultured overnight. Cells were serum-starved for 24 h and incubated with TGFβ (5 ng/mL) and different concentrations (50 nM, 100 nM) of ERA, 100 nM SPIONs, or ERA-SPIONs (equivalent to 100 nM ERA) for 24 h. Cells were lysed with RNA lysis buffer to perform quantitative real-time PCR analyses, with protein lysis buffer for western blot analyses, or fixed with acetone:methanol (1:1) for immunohistochemistry.

2.4.5. Migration

The effect of ERA and ERA-SPIONs on the migration of LX-2 cells was investigated in a scratch wound healing assay. Cells were seeded in 12-well plates ($5*10^4$ cells/well) and incubated overnight followed by overnight starvation with serum-free medium. Standardized scratches were made with a 10 μL pipette tip fixed in a holder. Subsequently, cells were washed and incubated with 1 mL of serum-free medium with or without TGFβ (5 μL/mL) in combination with ERA (50 nM, 100 nM), 100 nM SPIONs, or ERA-SPIONs (equivalent to 100 nM ERA). Images were taken at 0 and 24 h after treatment using a Nikon E400 microscope (Nikon). Images were analyzed using ImageJ to quantify the area of scratch represented as the percentage of wound closure relative to the control wells.

2.4.6. Contractility

The effect of ERA and ERA-SPIONs on the contractility of LX-2 cells was analyzed using 3D collagen gel matrix contraction assays. A collagen suspension (9 mL) containing 4.5 mL collagen G1 (5 mg/mL, Matrix biosciences, Morlenbach, Germany), 0.75 mL 10x M199 medium (Sigma), 127.5 μL 1 N NaOH (Sigma) and 2.1225 mL sterile water was prepared and then mixed with 1 mL ($2*10^6$) of LX-2 cells. Collagen gel-cell suspension (600 μL/well) was plated in a 24-well culture plate and allowed to polymerize for 1 h at 37 °C. Polymerized gels were incubated with 1 mL of serum-free medium with or without TGFβ (5 ng/mL) together with ERA (50 nM, 100 nM), 100 nM SPIONs, or ERA-SPIONs (equivalent to 100 nM ERA), followed by detachment of the gels from the culture wells. Digital images were taken after 72 h of treatment using a digital camera. The diameter of the gels was digitally measured using ImageJ and was normalized with their respective well size in each image and presented as relative gel contraction versus TGFβ-treated LX-2 cells.

2.5. In vivo biodistribution and therapeutic effect of ERA and ERA-SPIONs in an acute CCl_4-induced liver fibrosis mouse model

2.5.1. Biodistribution in an acute CCl_4-induced liver fibrosis mouse model

The in vivo biodistribution of ERA and ERA-SPIONs was investigated in an acute CCl_4-induced liver fibrosis mouse model. All the animal experiments were conducted strictly according to the ethical guidelines and regulations for the Care and Use of Laboratory Animals, Utrecht University, The Netherlands. The protocols were approved by the Institutional Animal Ethics Committee of the University of Twente, The Netherlands. All the animals received ad libitum non-fluorescent diet and normal water and were housed with a 12 h-light/12 h-dark cycle. 10-week-old male C57BL/6 mice (Janvier Labs) received a single intraperitoneal injection of 0.2 mL/kg carbon tetrachloride (CCl_4, Sigma), dissolved in olive oil, on day 1. CCl_4-treated mice were administered with one intravenous administration of ERA-Cy5.5 ($n = 5$), ERA-SPIONs-Cy5.5 ($n = 5$), or SPIONs-Cy5.5 ($n = 5$), with equivalent fluorescent intensity, 24 h after CCl_4 administration. The animals' abdomens were shaved, and near-infrared fluorescence was measured using the Pearl Trilogy Small Animal Imaging System (LI-COR Biosciences, Lincoln, NE) at 1, 4, and 24 h after intravenous administration, at ventral orientation and 255 μm resolution using the 700-channel laser source (excitation: 685 nm; emission: 720 nm) while the animals were anesthetized with isoflurane (2 %). Fluorescent signals were quantified using the Small Animal Image Analysis provided by Image Studio software (LI-COR Biosciences). Analysis exclusion criteria were incorrect shaving of the abdominal area, interfering with fluorescent signal ($n = 1$ in ERA-SPIONs-Cy5.5, $n = 1$ in SPIONs-Cy5.5). Animals were sacrificed after the 24-h imaging, and the harvested organs (liver, kidneys, spleen, lungs, and heart) were imaged to measure the fluorescent signal. Previously excluded animals (excluded due to incorrect shaving) were included since exclusion criteria did not impact organ fluorescent measurements. The liver and other organs were retrieved for further analyses.

2.5.2. In vivo therapeutic efficacy in an acute CCl_4-induced liver fibrosis mouse model

The in vivo therapeutic effect of ERA and ERA-SPIONs was investigated in an acute CCl_4-induced liver fibrosis mouse model. These animal experiments were performed in strict accordance with the guidelines and regulations for the Care and Use of Laboratory Animals, Utrecht University, The Netherlands. The protocols were approved by the Institutional Animal Ethics Committee of the University of Twente, The Netherlands. All the animals received ad libitum normal chow diet and normal water and were housed with a 12 h-light/12 h-dark cycle. Male C57BL/6 mice (8–10 weeks old, Janvier Labs) received a single intraperitoneal injection of 0.5 mL/kg CCl_4 (Sigma), dissolved in olive oil, on day 1. Healthy controls ($n = 5$) received olive oil, as a control for CCl_4. CCl_4-treated mice were treated with two intravenous (i.v.) administrations of PBS ($n = 5$), ERA (50 μg/kg, $n = 5$), or ERA-SPIONs (equivalent ERA dose 50 μg/kg, $n = 5$) on days 2 and 3. All the animals were euthanized on day 4 b y cervical dislocation. Blood (obtained via cardiac puncture) and liver tissues were retrieved for further analyses. All the animals were weighed before sacrificing, and the respective organs were weighed directly after sacrificing.

The frequency of administration was based on our previous study where we administered FGF2 or FGF2-SPIONs after 24 and 48 h following CCl_4 administration [42]. For dosing, we referred to the previous reports where Tanaka et al. compared different routes of administration (i.v. versus intraportal) of a mixed endothelin receptor antagonist (TAK-044) and found the liver concentration of TAK-044 (injected intravenously at the dose of 10 mg/kg) was highest in the i. v. group [61], while another study reported 1 mg/kg bolus i. v. injection of ABT-627 (ERA) [62]. In this study, we used a very low dosing consistent with another study, where the authors performed dose-finding analysis using 2 nM to 2 mM different ERAs [31].

2.5.3. Alanine aminotransferase activity

Heparinized whole blood samples of animals were centrifuged at 2300×g for 10 min at 4 °C. Plasma was transferred in new Eppendorf's and stored at −80 °C until further analysis. The alanine aminotransferase (ALT) activity was determined in the plasma samples using a colorimetric ALT activity assay kit (MAK052, Sigma) according to the manufacturer's instructions.

2.5.4. Sample preparation for gene and protein expression

The effect of ERA and ERA-SPIONs on gene expression was investigated in mouse liver tissues using quantitative real-time PCR. Tissues were grinded and lysed with RNA lysis buffer to perform quantitative real-time PCR analyses. The effect of ERA and ERA-SPIONs on protein expression was investigated histologically in liver tissues using (co) immuno (fluorescent) staining. Collected liver tissues were transferred to Tissue-Tek OCT embedding medium (Sakura Finetek, Torrance, CA, USA) and were snap-frozen in 2-methyl butane on dry ice. Cryosections (6 μm) were cut using a Leica CM 3050 cryostat (Leica Microsystems, Nussloch, Germany). The cryosections were air-dried and fixed with acetone for 20 min for immunohistochemical and immunofluorescent staining.

2.5.5. Ex vivo MRI

SPIONs provide a possibility for MRI-based diagnosis, therefore, we used MRI to detect ERA-SPIONs in liver tissues derived from the biodistribution study (refer to 2.5.1). Ex vivo MRI was performed on the formalin-fixed liver segments of the liver tissues from the in vivo biodistribution study (with a sample size of $n = 15$, comprising 5 mice per group) using a portable low-field MRI scanner system (Pure Devices, Rimpar, Germany) with a bore of 15 mm diameter at a field strength of 0.5 T [63]. This procedure was conducted while the tissue samples were immersed in formalin. The following 3D spin-echo images were acquired with a field-of-view $14 \times 14 \times 14\ mm^3$ and an isotropic resolution of 125 μm: (i) T1-weighted (T_1w): A non-quantitative MRI sequence less sensitive to SPIONs content; (ii) T2-weighted (T_2w): A non-quantitative MRI sequence sensitive to SPIONs content allowing for low detection limits; (iii) T2 map: To measure the multi-echo transverse relaxation time: An echo sequence was acquired with echo times ranging from 6.5 ms to 318.5 ms in 6.5 ms steps. The transverse relaxation time was evaluated voxel by voxel using mono-exponential decay [64,65]. The MRI results were compared across the three experimental groups: ERA, ERA-SPIONs, and SPIONs. MRI acquisition and processing was done using in-house developed software using MATLAB (2021a, MathWorks, Natick, MA, USA). Average signal intensity was calculated using the region of interest (ROI) for all three MRI sequences.

2.5.6. In vivo MRI

In vivo MRI was performed using a 9.4 T small animal magnetic resonance scanner with 20 cm bore size (BioSpec 94/20; Bruker BioSpin, Ettlingen, Germany) equipped with a 1 T/m gradient system and 35 mm volume coil (Rapid Biomedical, Rimpar, Germany). The system was operated using ParaVision 6.0.1. software (Bruker BioSpin, Ettlingen Germany), which provided a pulse program for 2D UTE (ultrashort echo time) MRI. The T2*map was recorded with a 2D UTE sequence. Scan parameters: repetition time (TR), 1800 ms; echo time (TE), 329–40000 μs; number of echos, 14; averages, 1; number of slices, 1 (coronal); slice thickness, 1.5 mm; matrix, 80 × 80 μm; field of view, 30 × 30 mm; respiration trigger, total scan time, 56 min. Analysis with custom script MATLAB R2023b for mono-exponential fitting of T2*. The gradient trajectory distortion was measured in a preceding scan and was used for reconstruction of all scans with identical geometry. Also, a dynamic scan (2D UTE at TE 3 ms) confirmed complete distribution of the nanoparticles after 30 min. A total of $n = 6$ animals (wild-type Balb/C mice, female, age 10–14 weeks under the animal ethics approval no. 81–02.04.2020. A194) was used for this study. Mice were anesthetized by isoflurane inhalation throughout the experiments (1–1.2 % in 1 L/min O_2) and respiration and body temperature were monitored and kept in the physiological range (37 ± 0.5 °C, respiration rate 80-90 breath per minute). T2* mapping was performed before and 30 min post injection of SPIONs ($n = 3$) or ERA-SPIONs ($n = 3$) (@150 μmol/kg Fe in 100 μL PBS, tail vein catheter 30G, 50 μmol/min).

2.6. Quantitative real-time PCR

Total RNA was extracted using GenElute Total RNA Miniprep Kit (Sigma) for LX-2 cells or SV total RNA isolation system (Promega Corporation, Fitchburg, WI, USA) for mouse liver tissues according to the manufacturer’s instructions. The RNA concentration was quantified using NanoDrop® ND-1000 Spectrophotometer (Thermo Scientific, Waltham, USA). Total RNA (1 μg) was reverse transcribed using iScript cDNA synthesis kit (Bio-Rad, Hercules, CA, USA) according to the manufacturer’s instructions. For quantitative real-time PCR, 20 ng cDNA was used for each PCR reaction and was performed with 2x SensiMix SYBR and Fluorescein Kit (Bioline GmbH, QT615-05, Luckenwalde, Germany) and pre-tested and gene-specific primers (see Supplementary Table 1), using a BioRad CXF-384 Real-Time PCR detection system (BioRad). Gene expression levels were determined and normalized against that of the housekeeping gene GAPDH.

2.7. Western blot analysis

Cells were lysed using 1x lysis buffer prepared from 3x blue loading buffer and 30x reducing agent (1.25 M dithiothreitol, DTT) (Cell Signaling Technology, Massachusetts, MA, USA) as per manufacturer’s instructions. Protein lysates were loaded on 10 % Tris-Glycine gel (Thermo Scientific) followed by transfer onto a PVDF membrane (Roche). The membranes were developed according to the standard protocols by incubation with the primary antibodies and secondary antibodies (see Supplementary Table 2). The protein bands were visualized using Pierce™ ECL Plus Western Blotting substrate (Thermo Scientific) and images were taken with FluorChem Imaging System. Intensities of individual bands were quantified using the NIH ImageJ software and the target protein expression levels were normalized to β-actin.

2.8. Immunohistochemistry

The cryosections (6 μm) were air-dried and fixed with acetone for 20 min for immunohistochemical and immunofluorescent staining. LX-2 cells were fixed with acetone:methanol (1:1) for 30 min at −20 °C, and air-dried for 30 min at room temperature. Tissue sections or cells were rehydrated with PBS and incubated with the primary antibody (α-SMA or Collagen-I, see Supplementary Table 2) overnight at 4 °C, followed by incubation with horseradish peroxidase (HRP)-conjugated secondary antibody for 1 h at room temperature. Endogenous peroxidase activity was blocked by 3 % H_2O_2 prepared in methanol. Subsequently, the tissue sections or cells were incubated with HRP-conjugated tertiary antibody for 1 h at room temperature. Peroxidase activity was obtained using 3-amino-9-ethyl carbazole (AEC, Thermo Scientific) for 20 min as per the manufacturer’s instructions. Thereafter, the tissue sections or cells were washed with MilliQ and counterstained with hematoxylin (Fluka Chemie, Buchs, Switzerland). Finally, the tissue sections and cells were mounted with Aquatex mounting medium (Merck). Images of tissue sections were made using the NanoZoomer (Hamamatsu, Japan), analyzed using ImageJ, and presented as relative expression versus CCl_4-treated tissue slides. Images of LX-2 cells were made using light microscopy (Nikon eclipse E600 microscope, Nikon), analyzed using ImageJ, and presented as relative expression versus TGFβ-treated LX-2 cells.

For co-immunohistochemical staining, the cryosections (6 μm) were air-dried and fixed with acetone for 10 min and air-dried for 30 min at room temperature. Tissue sections were rehydrated with PBS and endogenous peroxidase activity was blocked by 3 % H_2O_2 prepared in methanol. Subsequently, the tissue sections were washed with PBS and endogenous biotin was blocked with DAKO biotin blocking system (BioLegend, San Diego, CA), followed by incubation of Mouse on Mouse (M.O.M.) Mouse IgG blocking reagent (Vector Laboratories, Burlingame, CA) for 1 h. Sections were incubated with M.O.M. Diluent (Vector Laboratories), followed by incubation with the first primary antibodies (anti-PEG and anti-p-ERK, see Supplementary Table 2) prepared in M.O.M. diluent for 1 h at room temperature, followed by incubation with the second primary antibody (anti-α-SMA, Supplementary Table 2) prepared in M.O.M. diluent for 30 min at room temperature. This was subsequently followed by incubation with M.O.M. Biotinylated Anti-Mouse IgG reagent (Vector Laboratories) for 10 min at room temperature, followed by incubation with VECTASTAIN Elite ABC reagent (Vector Laboratories) for 5 min at room temperature. Sections were incubated with alkaline phosphatase-conjugated secondary antibody for 30 min at room temperature, followed by alkaline phosphatase-conjugated tertiary antibody for 30 min at room temperature, after which the sections were washed with tris-buffered saline (TBS). Alkaline phosphatase reaction was obtained using BCIP/NBT substrate (Sigma Aldrich) for 15 min at 37 °C. Peroxidase activity was obtained using AEC substrate for 20 min as per the manufacturer’s instructions. Thereafter, sections were extensively washed with tap water and finally, tissue sections were mounted with Aquatex mounting medium. Images of tissue sections were made using the NanoZoomer (Hamamatsu, Japan), analyzed using ImageJ, and presented as relative expression versus CCl_4-treated liver-sections.

2.9. Co-immunofluorescent staining

The cryosections (6 μm) were air-dried and fixed with acetone for 20 min. Tissue sections were rehydrated with PBS and incubated with the primary antibodies (anti-Collagen-I and anti-PEG, see Supplementary Table 2) overnight at 4 °C, followed by incubation with Alexa Fluor-conjugated secondary antibodies (AF-594 and AF-488, see Supplementary Table 2) for 1 h at room temperature. Finally, sections were mounted using a mounting medium with DAPI (Sigma). Slides were stored at 4 °C in the dark until imaging. Fluorescent images were made using a Nikon E400 microscope (Nikon). ImageJ was used to make the overlay images and to quantitate the fluorescent signal.

2.10. Statistical analyses

The graphs and statistical analyses were performed using GraphPad Prism (version 10.0.0, GraphPad Prism, La Jolla, CA, USA). Comparisons between two groups were performed using the unpaired students’ t-test and multiple comparisons between multiple groups were performed using one-way analysis of variance (ANOVA) with a Bonferroni post hoc test. The differences were considered significant when $^{*}p < 0.05$, $^{**}p < 0.01$, $^{***}p < 0.001$, $^{****}p < 0.0001$, respectively.

3. Results

3.1. ETAR expression is upregulated in cirrhotic human livers, fibrotic mouse livers, and TGFβ-activated hepatic stellate cells

We first examined the expression of endothelin-1 (ET-1; *EDN1*), endothelin A receptor (ETAR; *EDNRA*), and collagen-I, a fibrotic marker, in human cirrhotic livers using the publicly available human dataset GSE14323. Transcriptomic data analysis revealed a significant increase in the expression levels of ET-1 ($p < 0.001$) and ETAR ($p < 0.01$) in cirrhotic livers compared to healthy controls, as can be seen in Fig. 1A. In addition, a significant positive correlation ($p < 0.0001$) has been found between the expression of ET-1 and ETAR with collagen-I, a fibrosis marker (Fig. 1A). These results indicate that ET-1 and ETAR are upregulated in the liver of cirrhosis patients and that the expression of ET-1 and ETAR correlates with fibrosis progression.

Next, we examined the expression level of ET-1, ETAR, and different fibrosis-related genes in normal and acute CCl_4-induced fibrotic mouse livers and TGFβ-activated human HSCs (LX-2 cells). The gene expression levels of ET-1 (*Edn*), ETAR (*Ednra*), collagen type I α1 (*Col1a1*), smooth muscle actin alpha 2 (*Acta2*), desmin (*Des*), vimentin (*Vim*), tissue inhibitor of metalloproteinases 1 (*Timp1*), and platelet-derived growth factor receptor beta (*Pdgfrb*) were examined in acute CCl_4 mouse livers versus normal livers and in TGFβ-activated LX-2 cells versus control LX-2 cells. *COL1A1, ACTA2, DES, VIM, TIMP1,* and *PDGFRB* are HSCs-activation markers that are upregulated upon HSCs activation during fibrosis. The expression of ET-1 and ETAR was significantly upregulated in mice with acute CCl_4-induced liver fibrosis and in LX-2 cells (Fig. 1B and C). Correspondingly, the expression of activated HSC markers was significantly upregulated in acute CCl_4-treated livers and in TGFβ-activated LX-2 cells compared to healthy and non-activated controls respectively (Fig. 1B and C). Additionally, we examined the expression

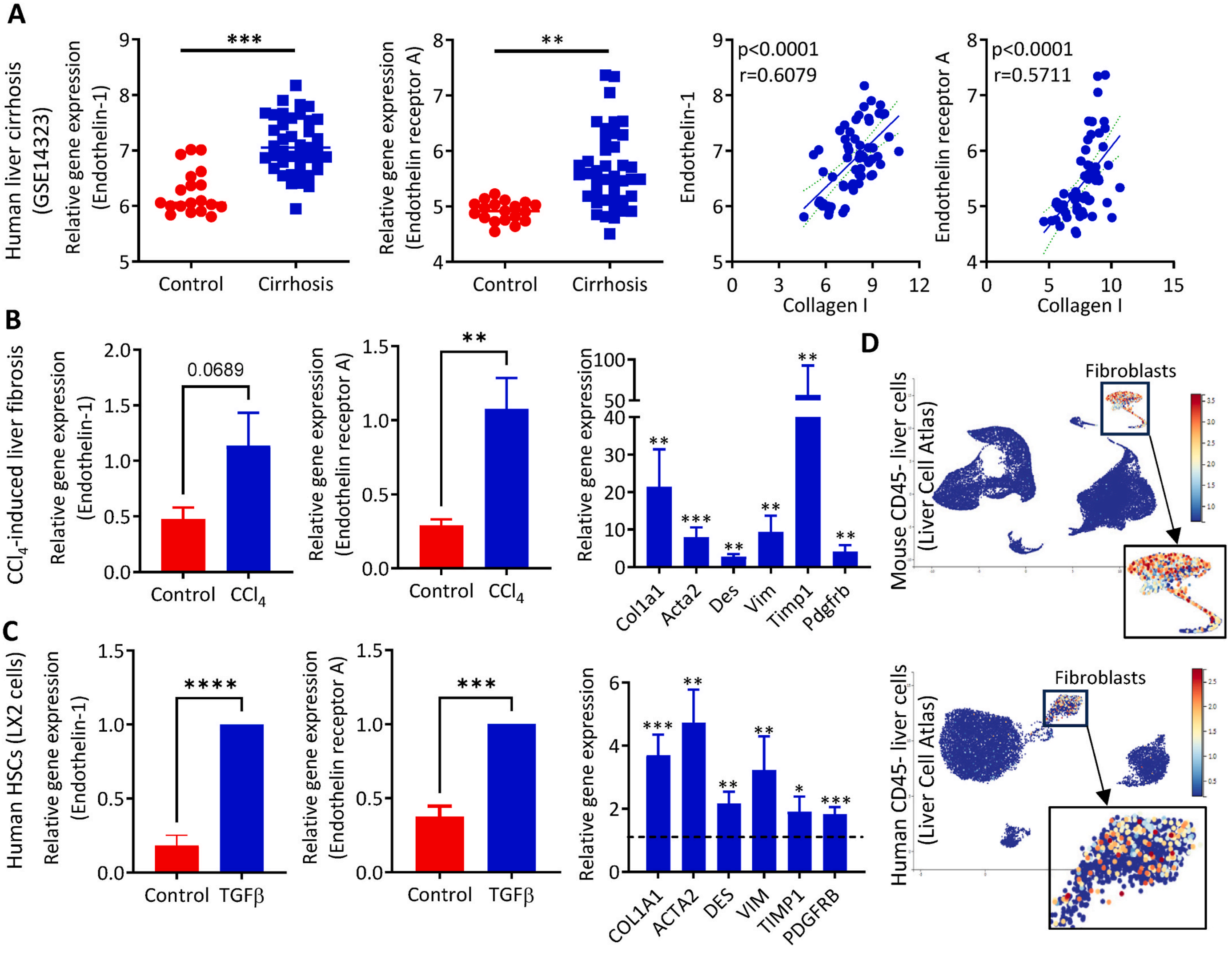

Fig. 1. Expression of endothelin-1 and endothelin A receptor in healthy and fibrotic human and mouse livers, and in activated hepatic stellate cells (HSCs). (**A**) Endothelin-1, endothelin A receptor, and collagen-I mRNA expression levels from publicly available human microarray dataset (GSE14323). Healthy livers ($n = 19$) and cirrhosis livers ($n = 41$). Correlation was made between mRNA data of endothelin-1 and collagen-I, and endothelin A receptor and collagen-I. (**B**) Relative mRNA expression of endothelin-1, endothelin A receptor, collagen type I α1 (*Col1a1*), actin alpha 2 (*Acta2*), desmin (*Des*), vimentin (*Vim*), tissue inhibitor of metalloproteinase 1 (*Timp1*), and platelet-derived growth factor receptor beta (*Pdgfrb*) in CCl_4 mouse livers ($n = 5$) versus healthy livers ($n = 5$). (**C**) Relative mRNA expression of endothelin-1, endothelin A receptor, *COL1A1, ACTA2, DES, VIM, TIMP1,* and *PDGFRB* in TGFβ-activated HSCs (LX-2 cells) ($n = 4$) versus unstimulated cells ($n = 4$). (**D**) Expression of endothelin A receptor on $CD45^-$ liver cells of human and mouse livers at the single cell level using the Liver Cell Atlas. Zoomed inserts are the single cells categorized as fibroblasts. Orange and red dots indicate enhanced expression. The information about the different clusters is provided in Supplementary Fig. S1. The data of all graphs are represented as mean + SEM. Comparisons with control groups were analyzed using unpaired students' t-test. The differences were considered significant for a p-value of $*p < 0.05$, $**p < 0.01$, $***p < 0.001$, $****p < 0.0001$.

of ETAR on ($CD45^-$) liver cells of humans and mice at a single cell level using the Liver Cell Atlas (Fig. 1D, Supplementary Fig. S1) [58]. We found that ETAR is solely expressed by the HSC/fibroblast population in humans as well as mice, indicated by the high-expression red/orange dots (Fig. 1D). Altogether, these results indicate that ET-1 and ETAR are upregulated in acute CCl_4-induced liver fibrosis and in TGFβ-activated LX-2 cells and correlate with liver fibrosis and HSC activation. Moreover, ETAR is specifically expressed on HSCs highlighting ETAR antagonism as an attractive approach to inhibit HSC activation and to ameliorate liver fibrosis.

3.2. ERA inhibited TGFβ-induced collagen-I and α-SMA expression, contractility, and migration in human HSCs (LX-2 cells) in vitro

In our study, we used an ETAR antagonist (CH948) derived from PD-156707, a potent and orally active nonpeptide ETAR-selective antagonist initially designed by Parke-Davis [51,52,59]. As mentioned previously, in CH948 one methoxy group is modified with an amino group using a PEG-spacer to enable coupling reactions [54]. The chemical structure of CH948 (ERA) is presented in Fig. 2A. We first investigated the therapeutic effect of ERA on TGFβ-induced HSC activation i.e., on the protein and gene expression of collagen-I *(COL1A1)* and α-SMA *(ACTA2)*. LX-2 cells were activated using 5 ng/mL TGFβ and simultaneously incubated with 50 nM and 100 nM ERA. TGFβ-induced upregulation in *COL1A1* (3.6-fold increase, $p < 0.0001$), *ACTA2* (2.4-fold increase, $p < 0.001$), and *TIMP1* (2.5-fold increase, $p < 0.0001$) mRNA expression compared to control LX-2 cells. After treatment with ERA, the TGFβ-induced expression of *COL1A1*, *ACTA2*, and *TIMP1* was significantly inhibited in a concentration-dependent manner (Fig. 2B). Moreover, at the protein level, immunohistochemical staining and western blot confirmed that ERA dose-dependently attenuated TGFβ-induced collagen-I and α-SMA protein expression in LX-2 cells (Fig. 2C and D).

Activated HSCs, upon TGFβ activation, become highly migratory and contractile cells driving fibrogenesis [4,6]. We examined the effect of ERA on TGFβ-induced HSC contraction and migration using a 3D-collagen matrix contraction assay and a scratch assay, respectively. We found that TGFβ potentiated contraction of HSCs (1.5-fold increase, $p < 0.0001$) while ERA (at 100 nM) significantly inhibited TGFβ-induced contraction (1.3-fold decrease, $p < 0.01$) (Fig. 2E and F). Furthermore, we observed that ERA dose-dependently hampered TGFβ-induced HSC migration (Fig. 2G and Supplementary Fig. S2). Finally, we analyzed the effect of increasing concentrations of ERA on cell metabolic activity (Fig. 2H). TGFβ enhances HSC proliferation, explaining the significant difference in metabolic activity between control and TGFβ-activated HSCs (1.4-fold increase, $p < 0.0001$). Cell metabolic activity was not affected upon treatment with ERA, suggesting that ERA has no cytotoxic effects at 50 and 100 nM concentrations.

These results together indicate the ERA (CH948) inhibits TGFβ-induced HSC activation most likely by antagonizing ETAR, specifically expressed on HSCs.

3.3. Successful conjugation of ERA to SPIONs

Antagonism of the ETAR pathway using small-molecule ERAs can result in limited therapeutic effects due to poor pharmacokinetics and rapid clearance [34]. High or frequent dosing will be required to achieve desired therapeutic effects, which might result in adverse (off-target) effects. In this study, we conjugated ERA to SPIONs to improve the pharmacokinetic profile of ERA and to increase hepatic uptake thereby eliminating the need for high or frequent dosing, while increasing the therapeutic efficacy by increasing the effective concentration of ERA in the liver.

ERA was conjugated to dextran-coated PEG-COOH functionalized SPIONs via COOH groups using carbodiimide chemistry, as illustrated in Fig. 3A. The successful conjugation of the ERA to SPIONs was confirmed by HPLC, FTIR spectroscopy, and MALDI-TOF mass spectrometry. Physicochemical properties (size and zeta potential) of ERA-SPIONs and SPIONs were determined using DLS, and the magnetic properties of ERA-SPIONs versus SPIONs were examined by VSM.

HPLC analysis of starting concentrations of ERA and unreacted ERA in the wash solutions collected during purification while conjugating ERA to SPIONs revealed a conjugation efficacy of approx. 94 % (Table 2). FTIR spectra were analyzed for specific ERA signals by comparing the ERA-SPIONs spectrum with the spectra of unmodified SPIONs and glycine-SPIONs (Supplementary Fig. S3). Although all spectra were dominated by dextran and PEG coating contributions, distinct peaks were visible between 1900 cm^{-1} and 2200 cm^{-1} of ERA-SPIONs (region indicated with a box) which could be attributed to the γ-hydroxy-butenolide core of CH948 [66]. Furthermore, MALDI spectra were obtained for SPIONs with and without ERA conjugation. Based on the molecular weight of the individual peaks of the spectrum, the identity of conjugated molecules could be confirmed. As shown in Fig. 3B, ERA-SPIONs revealed peaks in the spectra 500–900 m/z i.e., peaks at 650 and 666/667 m/z that correspond to the fragments of CH948, of which the chemical structures are depicted in Supplementary Fig. S4. Collectively, HPLC, FTIR, and MALDI-TOF measurements suggest the successful conjugation of ERA (CH948) to the SPIONs.

Next, we performed DLS measurements of (unmodified) SPIONs and ERA-SPIONs, which revealed an increase in the hydrodynamic size of SPIONs after ERA conjugation (approx. 9 nm in MilliQ water and 35 nm in PBS) and a change in the zeta-potential (from −0.42 to −6.49 mV). We compared the DLS measurements of ERA-SPIONs with glycine-SPIONs which showed an increase in the hydrodynamic size of approx. 4 nm in MilliQ water and 24 nm in PBS, while no major change in the zeta-potential (−6.49 to −6.86 mV) was observed (Fig. 3C and Table 1). Both glycine-SPIONs and ERA-SPIONs showed a low-to-acceptable polydispersity index (PdI) (though higher than SPIONs) suggest relatively monodisperse particles. These results showing the increase in the hydrodynamic size and decrease in the zeta potential compared to SPIONs further confirm the conjugation of ERA (and/glycine) to SPIONs. Glycine-SPIONs were used as a control to confirm the DLS results of ERA-SPIONs versus (unmodified) SPIONs. Additionally, the monodispersity, core size, and morphology of the ERA-SPIONs were visualized using transmission electron microscopy (TEM) and scanning (transmission) electron microscopy [S(t)EM] (Fig. 3D and Supplementary Figs. S5A and B). We performed compositional analysis and elemental mapping of SPIONs and ERA-SPIONs using Energy Dispersive X-ray spectroscopy (EDX). STEM-EDX maps confirm the presence and homogenous distribution of iron and oxygen (iron oxide core) in the particles (Fig. 3E and Supplementary Fig. S5C).

We also evaluated the stability of the ERA-SPIONs by re-measuring the hydrodynamic size and zeta potential of the ERA-SPIONs after 4 months of storage at 4 °C. We observed an increase in the hydrodynamic size (approx. 31 nm in MilliQ and 61 nm in PBS with a low-to-acceptable PdI) indicating a low degree of aggregation of the ERA-SPIONs after 4 months of storage, while no significant change in the zeta potential was found (Supplementary Table 3) suggesting that the ERA-SPIONs are relatively stable after 4 months of storage at 4 °C.

Additionally, we evaluated the stability of the nanoparticles by measuring the hydrodynamic size of SPIONs and ERA-SPIONs in different physiological media with and without FBS at 37 °C (Supplementary Table 4). The results showed higher PdI in the FBS-containing media due to the presence of additional peaks in these samples. This most likely is caused by the particles present in the FBS as can be also seen in the DLS measurements in the only medium controls. These data suggest that SPIONs and ERA-SPIONs are stable in different physiological media during physiological temperatures.

Besides estimating the ERA concentration, we also determined the iron concentration of the SPIONs in ERA-SPIONs using calorimetric Prussian blue assay (Supplementary Fig. S6A). Using the standard curve prepared from the known concentrations of iron, we found that the concentration of ERA-SPIONs after conjugation was 1.75 ± 0.05 mg/

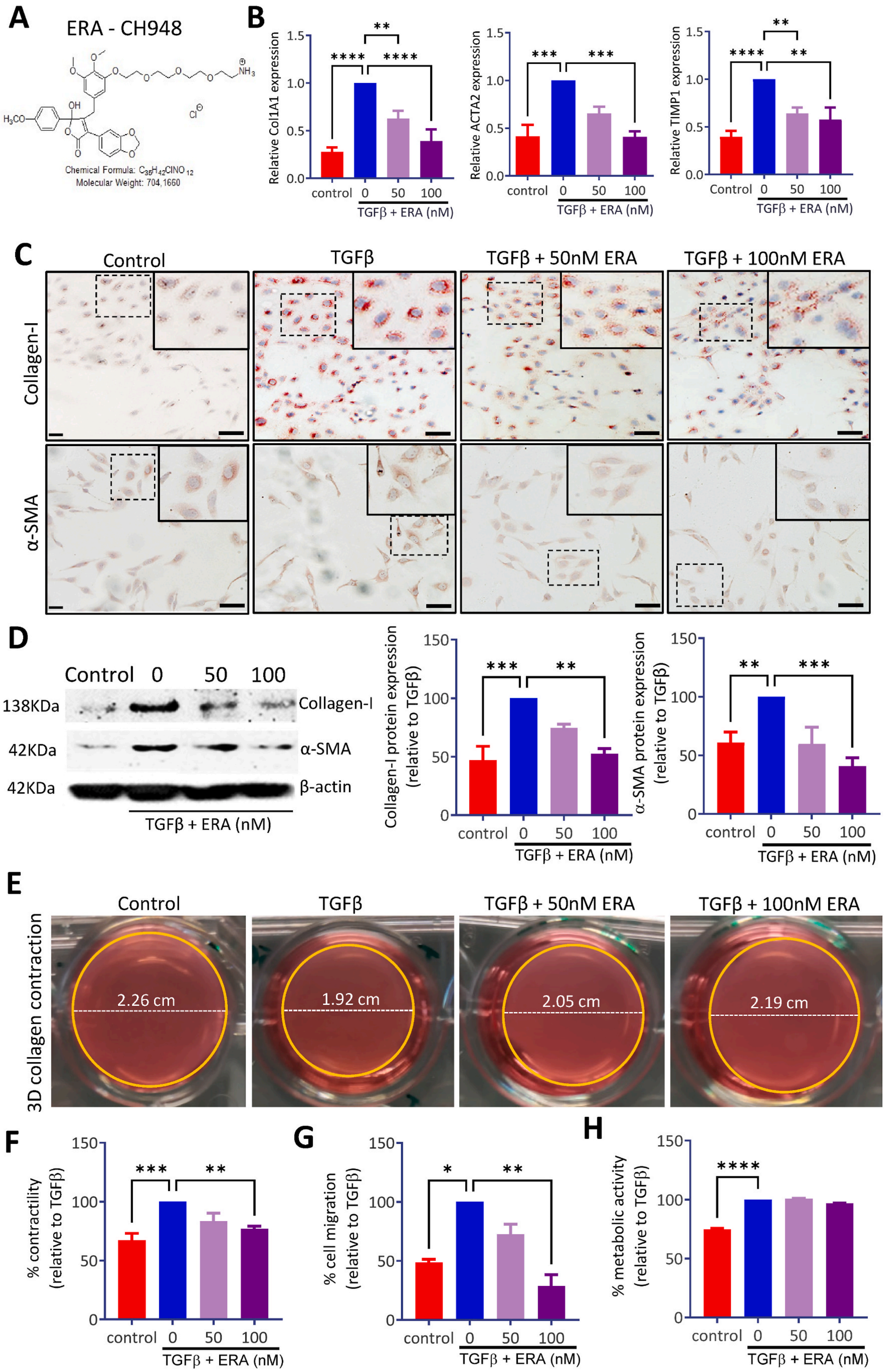

(caption on next page)

Fig. 2. Effect of different concentrations of ERA on TGFβ-induced collagen-I and α-SMA expression, contractility, and migration in human HSCs versus control (unstimulated) cells. (**A**) Chemical structure of ERA (CH948). (**B**) Relative mRNA expression (normalized to *GAPDH*) of *COL1A1*, *ACTA2*, and *TIMP1* (relative to TGFβ). (**C**) Representative images (scalebar = 100 μm) and zoom-ins (scalebar = 200 μm) showing immunohistochemical staining of collagen-I and α-SMA. (**D**) Western blot depicting bands for collagen-I, α-SMA, and β-actin and relative quantified protein expression (relative to TGFβ) of collagen-I and α-SMA (normalized by β-actin) obtained by western blot. (**E**) Representative images of 3D-collagen contraction assay (after 72 h) with the diameters of collagen gels (in cm). (**F**) Quantitative analysis of 3D-collagen contraction assay expressed in percentages (relative to TGFβ). (**G**) Quantitative analysis (after 24 h) of wound healing assay (relative to TGFβ). Representative images are provided in Supplementary Fig. S2. (**H**) Metabolic activity (relative to TGFβ). The data are represented as mean + SEM. All experiments were conducted at least three times to be able to make statistical comparisons. Multiple comparisons between different groups were performed by one-way analysis of variance (ANOVA) with a Bonferroni post hoc test. The differences were considered significant for a p-value of *$p < 0.05$, **$p < 0.01$, ***$p < 0.001$, ****$p < 0.0001$.

mL. The lower iron concentration in ERA-SPIONs (about 27 %) than the starting SPIONs concentration is attributed to the loss of SPIONs during several purification steps in the conjugation reactions. No Prussian blue/iron was detected in ERA alone.

The magnetic properties of the ERA-SPIONs versus SPIONs were analyzed using VSM at room temperature. The magnetization (M − H) curves denoted by magnetization (M) versus magnetic field (H) of ERA-SPIONs and SPIONs affirm the superparamagnetic properties of ERA-SPIONs and SPIONs (Supplementary Fig. S6B). The saturation magnetization (Ms) of ERA-SPIONs was measured as 62 emu/g iron which is slightly lower than unmodified SPIONs (66 emu/g iron). The lower Ms values of ERA-SPIONs can be ascribed to the size and surface modification of SPIONs with non-magnetic ERA.

Lastly, we determined the relaxivity constants (r_1 and r_2) of both SPIONs and ERA-SPIONs in the 0.5 T MRI system and the 9.4 T MRI system (Supplementary Fig. S6C), since relaxivity measurements are strongly field dependent [67]. At 0.5 T, the longitudinal (26.08 vs 26.18 L/mmol-s) and transverse (193.1 vs 191.4 L/mmol-s) relaxation constants were comparable between SPIONs and ERA-SPIONs. At 9.4 T, the longitudinal (0.6988 vs 0.5559 L/mmol-s) and transverse (153.6 vs 122.8 L/mmol-s) relaxivities were higher for SPIONs compared to ERA-SPIONs. These results indicate that both SPIONs and ERA-SPIONs are MRI-detectable, at different magnetic field strengths, especially using T2* mapping.

Altogether, these results suggest the successful synthesis of ERA-SPIONs with favorable size, charge, and magnetic properties.

3.4. ERA-SPIONs inhibited TGFβ-induced HSCs activation in vitro

For the in vitro studies, 100 nM concentration of ERA and ERA-SPIONs (equivalent concentration of ERA based on ERA-conjugation efficiency) was used as ERA (100 nM showed the most significant effects in inhibiting HSC activation (Fig. 2).

We first investigated the binding ability of ERA-SPIONs to HSCs using Prussian blue staining. ERA-SPIONs showed a weak binding to non-activated HSCs and strong binding to TGFβ-activated HSCs while SPIONs alone did not bind to non-activated HSCs, however had a weak binding to activated HSCs (Supplementary Fig. S7). These data suggest that ERA-SPIONs interact with HSCs via TGFβ-induced ETAR, indicating that the conjugation of ERA to SPIONs retained its receptor binding activity.

After confirming the binding of ERA-SPIONs to activated HSCs, we focused on the pharmacological effects of ERA-SPIONs versus ERA and SPIONs. First, we examined the effects of ERA-SPIONs on the protein expression of collagen-I and α-SMA on TGFβ-activated LX-2 cells using immunohistochemical staining and western blots. We observed that ERA and ERA-SPIONs significantly inhibited TGFβ-induced collagen-I (2.3-fold decrease, $p < 0.01$ and 4.3-fold decrease, $p < 0.001$ respectively) and α-SMA (1.7-fold decrease, $p < 0.05$ and 2.5-fold decrease, $p < 0.01$ respectively) protein expression (Fig. 4A–C). Thereafter, we investigated the effects of ERA-SPIONs on gene expression of major HSC-activation markers i.e., *COL1A1*, *ACTA2,* and *TIMP1*. Treatment with ERA and ERA-SPIONs strongly reduced the expression of *COL1A1* (1.7-fold decrease, $p < 0.05$ and 3.2-fold decrease, $p < 0.001$ respectively), *ACTA2* (1.9-fold decrease, $p < 0.05$ and 3.4-fold decrease, $p < 0.001$ respectively), and *TIMP1* (1.6-fold decrease, $p < 0.05$ and 1.9-fold decrease, $p < 0.01$ respectively) (Fig. 4D).

Next, we investigated the effect of ERA-SPIONs on functional assays i.e., TGFβ-induced HSC migration and contraction. We found that ERA and ERA-SPIONs significantly decreased TGFβ-induced HSC migration (1.5-fold decrease, $p < 0.05$ and 2.0-fold decrease, $p < 0.01$ respectively) (Fig. 4E and Supplementary Fig. S8). Furthermore, we observed that the TGFβ-induced HSC contractility was significantly inhibited by ERA and ERA-SPIONs (1.4-fold decrease, $p < 0.05$ and 1.5-fold decrease, $p < 0.01$ respectively) (Fig. 4F and Supplementary Fig. S9). ERA-SPIONs showed higher therapeutic efficacy compared to ERA while SPION treatment did not affect TGFβ-induced HSC activation parameters. These results together indicate that the conjugation of ERA to SPIONs retained its pharmacological activity.

Finally, we also analyzed the effect of ERA, ERA-SPIONs, and SPIONs on the metabolic activity of LX-2 cells. As can be seen in Supplementary Fig. S9, TGFβ increased the metabolic activity of the cells due to increased LX-2 cell proliferation while ERA, ERA-SPIONs, or SPIONs evidenced no change in the metabolic activity, indicating that ERA, ERA-SPIONs, or SPIONs do not induce any cytotoxicity (Supplementary Fig. S9).

3.5. Increased liver uptake of ERA-SPIONs versus ERA in an acute CCl_4-induced liver injury mouse model

To investigate the hepatic uptake of ERA-SPIONs, we performed a biodistribution study in an acute CCl_4-induced liver injury/early fibrosis mouse model. To visualize ERA, SPIONs, and ERA-SPIONs during in vivo biodistribution, ERA-Cy5.5, SPIONs-Cy5.5, and ERA-SPIONs-Cy5.5 were prepared as per the methods described previously (refer to the methods section 2.2). The chemical structures of ERA-Cy5.5, ERA-PEG-NH_2, and Cy5.5-NH_2 used for the preparation of ERA-SPIONs and/or ERA-SPIONs-Cy5.5 are presented in Supplementary Fig. S10A. Size and zeta potential measurements of the SPIONs-Cy5.5 and ERA-SPIONs-Cy5.5 were performed to confirm the successful conjugation of Cy5.5 or/and ERA to the SPIONs (Table 3 and Supplementary Fig. S10B). DLS measurements (Table 3) depict an increase in the hydrodynamic size of SPIONs-Cy5.5 (approx. 15 nm in MilliQ water and 27 nm in PBS) and ERA-SPIONs-Cy5.5 (approx. 26 nm in PBS) compared to glycine-SPIONs (Table 1). The change in the zeta potential, compared to the glycine-SPIONs, was observed for SPIONs-Cy5.5 (from −6.9 to −3.0 mV) following Cy5.5 conjugation and for ERA-SPIONs-Cy5.5 showed (from −6.9 to −7.4 mV) after ERA and Cy5.5 conjugation (Supplementary Fig. S10B and Tables 1 and 2). SPIONs-Cy5.5 and ERA-SPIONs-Cy5.5 showed low-to-acceptable PdI suggesting monodisperse particles. Additionally, the monodispersity, core size, and morphology of the ERA-SPIONs were visualized using SEM (Supplementary Fig. S10C).

Finally, we measured the fluorescence intensity of SPIONs-Cy5.5, ERA-SPIONs-Cy5.5, ERA-Cy5.5, and Cy5.5 (following serial dilutions) using the NIR imager to confirm the successful conjugation of Cy5.5 (with and without ERA) to the SPIONs, to compare the fluorescence intensities of SPIONs-Cy5.5, ERA-SPIONs-Cy5.5 and ERA-Cy5.5, and to ascertain no loss in fluorescence intensity due to quenching (Supplementary Fig. S10D). These results indicate the successful synthesis of SPIONs-Cy5.5 and ERA-SPIONs-Cy5.5 with comparable fluorescence

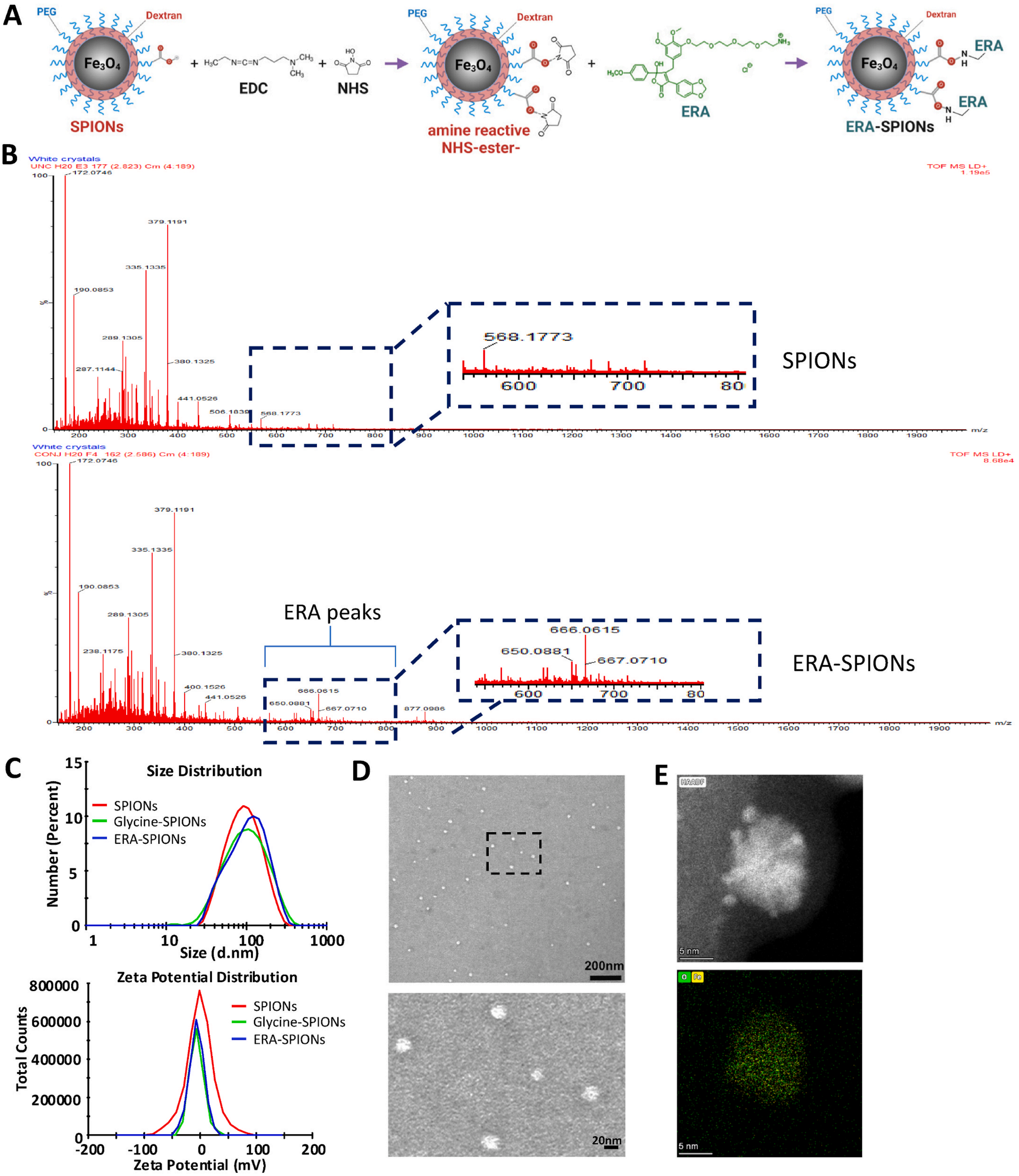

Fig. 3. Conjugation and characterization of ERA-SPIONs. (**A**) Schematic representation of ERA conjugation to SPIONs using carbodiimide chemistry. (**B**) MALDI-TOF spectra of SPIONs with and without ERA conjugation and zoomed in at ERA-corresponding peaks. Refer to Supplementary Fig. S4 for the chemical structures of ERA derivatives corresponding with peaks 650 and 666 *m/z*. (**C**) Graphs showing the hydrodynamic size distribution (in PBS) and zeta potential of (unmodified) SPIONs, glycine-SPIONs, and ERA-SPIONs. Refer to Table 1 for the summarized results. (**D**) Transmission electron microscopy (TEM) image (scalebar = 200 nm) and zoom of ERA-SPIONs (scalebar = 20 nm). (**E**) High Angle Annular Dark Field (HAADF) TEM image and Energy Dispersive X-ray (EDX) elemental mapping of iron (yellow) and oxygen (green) of an ERA-SPION.

Table 1
The physicochemical properties of SPIONs and ERA-SPIONs.

Nanoparticles	Size by number in MilliQ water (d.nm ± SD)	Polydispersity index (PdI ± SD)	Size by number in PBS (d.nm ± SD)	Polydispersity index (PdI ± SD)	ζ potential in KCl (mV ± SD)
SPIONs	79.9 ± 0.1	0.187 ± 0.013	79.4 ± 0.8	0.210 ± 0.006	−0.42 ± 0.47
ERA-SPIONs	88.6 ± 0.5	0.289 ± 0.032	114.3 ± 1.3	0.392 ± 0.004	−6.49 ± 0.07
Glycine-SPIONs	85.1 ± 5.4	0.288 ± 0.013	90.0 ± 2.33	0.308 ± 0.040	−6.86 ± 0.53

Table 2
The coupling efficiency of ERA to the SPIONs.

Sample	ERA (nmol)	Percentage of total ERA (%)
ERA concentration (starting)	10.66	100
ERA concentration in washing solution	0.67	6.24
ERA concentration in ERA-SPIONs	9.99	93.76

intensities of ERA-Cy5.5.

The schematic overview of the biodistribution study is depicted in Fig. 5A. Briefly, 24 h after CCl_4 administration, mice were intravenously injected with equivalent near-infrared fluorescence units of ERA-Cy5.5, SPIONs-Cy5.5, or ERA-SPIONs-Cy5.5. Animals were imaged 1, 4, and 24 h after administration of the Cy5.5-conjugates (Fig. 5B and Supplementary Fig. S11). The quantified fluorescent signal of ERA-SPIONs-Cy5.5 showed a high fluorescent signal 1 h after administration (880.5 ± 175.7 a. u.) with a slow decrease of the signal at 4 h (724.8 ± 97.66 a. u.) and 24 h (675.0 ± 144.6 a. u.), which was at all three time points significantly higher than ERA-Cy5.5 (62.98 ± 42.38 a. u., $p < 0.01$; 129.2 ± 82.97 a. u., $p < 0.01$; 16.43 ± 16.14 a. u., $p < 0.05$ respectively) (Fig. 5B and Supplementary Fig. S11). Directly after the last imaging time point (24 h), the animals were sacrificed and the fluorescent signal of the liver, kidneys, spleen, lungs, and heart was measured (Fig. 5C and D and Supplementary Fig. S11). The quantified signal showed a significantly higher uptake of ERA-SPIONs-Cy5.5 in the liver (4.3-fold, $p < 0.001$) compared to ERA-Cy5.5 (Fig. 5D and Supplementary Fig. S11). Additionally, we detected ERA-SPIONs-Cy5.5 uptake in kidneys (983.0 ± 78.8 a. u.) and spleen (332.8 ± 56.7 a. u.), however, compared to the signal of the liver (7666 ± 816.2 a. u.), the uptake in other organs was limited. The fluorescent signal over time as well as in the different organs of SPIONs-Cy5.5 was comparable to ERA-SPIONs-Cy5.5 (Fig. 5B–D and Supplementary Fig. S11), indicating that conjugation to the SPIONs facilitated increased hepatic uptake of ERA. Next, we analyzed cell-specific localization of ERA-SPIONs-Cy5.5 using co-immunostainings where ERA-SPIONs-Cy5.5 were detected using PEG staining. Results show the colocalization of ERA-SPIONs with α-SMA (a HSC marker) and collagen-I (a major ECM protein) (Supplementary Figs. S12 and S13), indicating selective binding of ERA-SPIONs to fibrotic areas specifically to (activated) HSCs. These results together suggest that the conjugation of ERA to SPIONs increases the hepatic uptake of ERA, which colocalizes to HSC-rich fibrotic areas in vivo.

Additionally, to confirm the ETAR antagonism by ERA-SPIONs, we analyzed ET-1/ETAR downstream signaling pathway (p-ERK) in the liver sections by co-immunostainings with p-ERK and α-SMA antibodies followed by p-ERK staining quantification (Supplementary Fig. S14). We observed decrease in total p-ERK expression (2.3–2.5-fold decrease) in the liver sections of ERA-SPIONs-Cy5.5 treated mice compared to the liver sections of SPIONs-Cy5.5 treated mice and ERA-Cy5.5 treated mice, indicative of ETAR antagonism by ERA-SPIONs (and not by ERA and SPIONs) treatment during liver injury.

3.6. MRI-detectable ERA-SPIONs in an acute CCl_4-induced liver fibrosis mouse model

SPIONs have been proved to accumulate easily in the liver and can be used as contrast agents in magnetic resonance imaging. To show the applicability of our engineered ERA-SPIONs for in vivo liver magnetic resonance imaging (MRI), a feasibility study in wild type mice was performed (Fig. 6). Briefly balb/c mice were anesthetized and were placed in the MRI scanner. SPIONs and ERA-SPIONs were intravenously administered via catheter and were immediately imaged after administration as per the methods detailed in the materials and methods section (Fig. 6A). Representation of the abdominal region with organ positioning (lung, gall bladder, and liver) and the imaging slice for T2* mapping and dynamic scanning is depicted in Fig. 6B. T2*-mapping of liver tissue showed a reduction in the values after injection of SPIONs (1.41 ± 0.19 ms vs. 6.24 ± 0.73 ms) and ERA-SPIONs (1.31 ± 0.27 ms vs. 5.20 ± 1.52 ms) (Fig. 6C and D and Supplementary Fig. S15). Signal intensity loss observed by dynamic imaging (Fig. 6E and Supplementary Fig. S16), further confirmed liver uptake. These results indicating immediate accumulation of the nanoparticles in the liver thereby confirming in vivo MRI detectability. In pursuit of our ultimate goal to develop a versatile targeted theranostic nanomedicine for multimodal imaging (optical/photoacoustic/MRI) and therapy (targeted therapeutic) for liver fibrosis, we assessed the MRI to detect the ERA-SPIONs in liver tissues of a CCl_4-induced acute liver injury-early liver fibrosis mouse model. Formalin-fixed liver tissue samples, obtained from the biodistribution study, were imaged using a portable low-field MRI scanner system (Fig. 7A). The results demonstrated the qualitative presence of SPIONs (visible as the low-intensity conglomerations of pixels observed in three different MRI sequences) resulting in less-bright (T_1w) or dark-appearing (T_2w and T_2 map) areas within the MRI. In contrast, ERA-treated tissue did not exhibit such dark areas (Fig. 7B). Quantitative analysis of the T_1w, T_2w, and T_2 map images indicated that both ERA-SPIONs and SPIONs displayed significantly low-MRI signals, with the intensity range appearing to be saturated due to the presence of high amounts of SPIONs in the livers (Fig. 7C). These findings together clearly demonstrate the MRI detectability of (ERA)-SPIONs in vivo.

3.7. ERA-SPIONs improved acute CCl_4-induced liver fibrosis in a mouse model

After confirming higher hepatic and HSCs-specific uptake of ERA-SPIONs, and confirming previous in vitro therapeutic findings, we subsequently investigated the therapeutic effects of ERA-SPIONs in vivo in an acute CCl_4-induced liver injury-early liver fibrosis mouse model. The schematic overview of the in vivo study can be visualized in Fig. 8A. Following CCl_4 administration, mice were treated with free ERA or ERA-SPIONs. Free SPIONs were not included in our in vivo studies since we have previously demonstrated that multiple intravenous administrations of SPIONs showed no therapeutic effect in vivo in CCl_4-treated mice, in accordance with our in vitro results [45]. Here, we first investigated the effect of ERA-SPIONs on organ weights normalized to body weight (Fig. 8B and Supplementary Fig. S17). Acute CCl_4 administration resulted in significantly increased liver weight respective to body weight (1.3-fold increase, $p < 0.0001$) (Fig. 8B). CCl_4 mice treated with free ERA (1.1-fold decrease, $p < 0.05$) and ERA-SPIONs (1.3-fold decrease, p

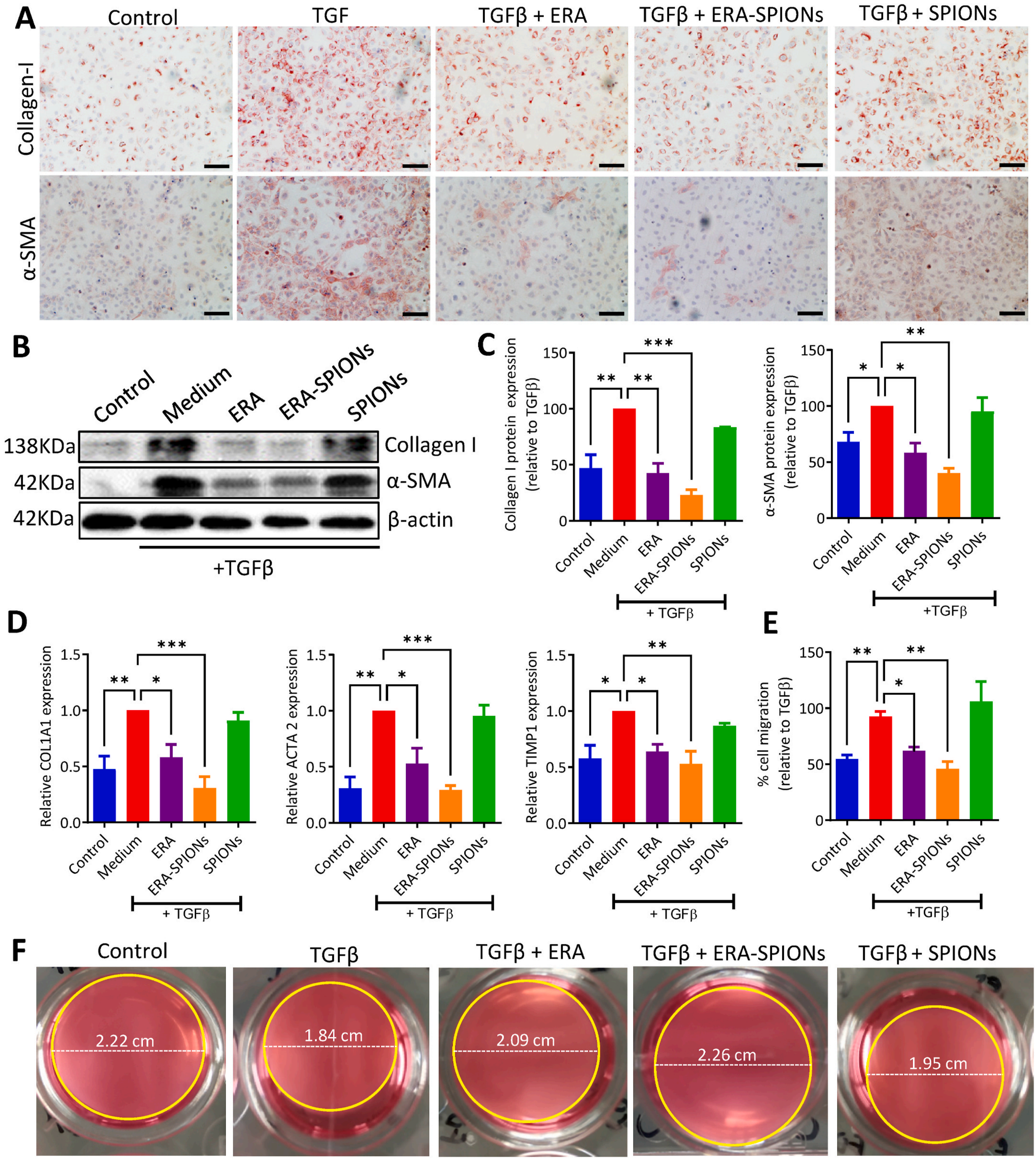

Fig. 4. Effect of ERA, ERA-SPIONs, and SPIONs on TGFβ-induced collagen-I and α-SMA expression, contractility, and migration in human HSCs versus control (unstimulated) cells. (**A**) Representative images (scalebar = 100 μm) of immunohistochemical staining of collagen-I and α-SMA. (**B**) Western blot depicting bands for Collagen-I, α-SMA, and β-actin. (**C**) Quantified expression (relative to TGFβ) of collagen-I and α-SMA signal (normalized to β-actin) obtained by western blot. (**D**) mRNA expression (relative to TGFβ, normalized to *GAPDH*) of *COL1A1*, *ACTA2*, and *TIMP1*. (**E**) Quantitative analysis (after 24 h) of wound healing assay (normalized to TGFβ control). Refer to the representative images provided in Supplementary Fig. S8. (**F**) Representative images of 3D-collagen contraction assay (after 72 h) with diameters of collagen gels (in cm). Refer to the quantitative analysis of the 3D-collagen contraction assay provided in Supplementary Fig. S9. The data are represented as mean + SEM. All experiments were conducted at least three times to be able to make statistical comparisons. Multiple comparisons between different groups were performed by one-way analysis of variance (ANOVA) with a Bonferroni post hoc test. The differences were considered significant for a p-value of $^{*}p < 0.05$, $^{**}p < 0.01$, $^{***}p < 0.001$.

Table 3
The physicochemical properties of SPIONs-Cy5.5 and ERA-SPIONs-Cy5.5

Nanoparticles	Size by number in MilliQ water (d.nm ± SD)	Polydispersity index (PdI ± SD)	Size by number in PBS (d.nm ± SD)	Polydispersity index (PdI ± SD)	ζ potential in KCl (mV ± SD)
SPIONs-Cy5.5	100.0 ± 0.8	0.285 ± 0.026	117.0 ± 1.1	0.306 ± 0.045	−3.0 ± 1.9
ERA-SPIONs-Cy5.5	84.8 ± 2.0	0.208 ± 0.009	115.7 ± 8.5	0.296 ± 0.041	−7.4 ± 1.5

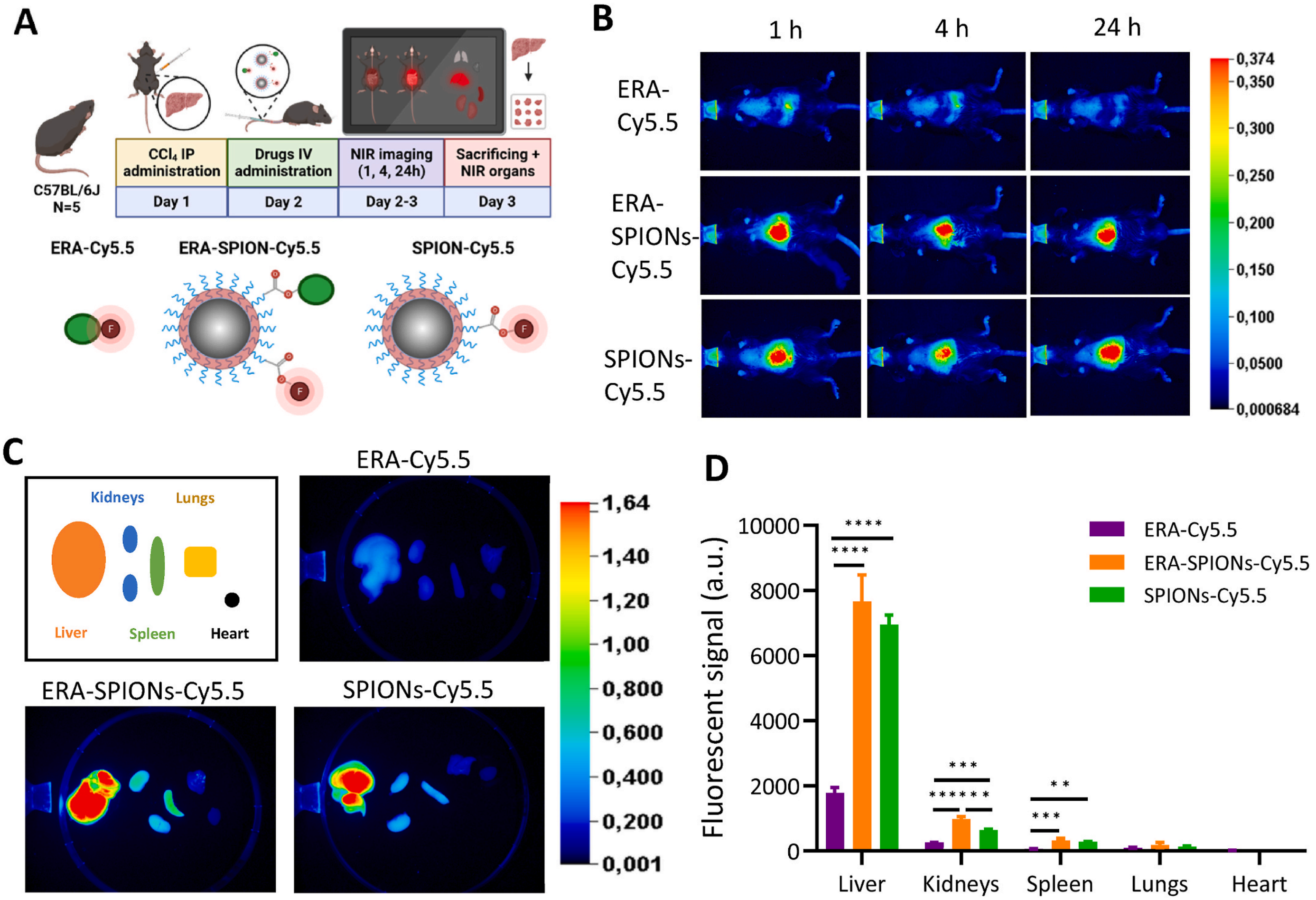

Fig. 5. Biodistribution of ERA-Cy5.5, ERA-SPIONs-Cy5.5, and SPIONs-Cy5.5 in CCl_4-induced acute liver injury mouse model. (**A**) Schematic of the regimen of biodistribution study. Refer to the data provided in Supplementary Fig. S10 and Table 3 showing the successful synthesis of SPIONs-Cy5.5, and ERA-SPIONs-Cy5.5. (**B**) Representative images of fluorescent signals after 1, 4, and 24 h of administration. Refer to the complete set of images provided in Supplementary Fig. S11. (**C**) Representative images of fluorescent signals in the liver, kidneys, spleen, lungs, and heart. (**D**) Quantified fluorescent signals in different organs. Refer to the complete set of images and quantitative image analysis provided in Supplementary Fig. S11. The data are represented as mean + SEM. Multiple comparisons between different groups (n = 5 per group) were performed by one-way analysis of variance (ANOVA) with a Bonferroni post hoc test. The differences were considered significant for a p-value of $^{**}p < 0.01$, $^{***}p < 0.001$, $^{****}p < 0.0001$.

< 0.0001) showed a significant decrease in normalized liver weight when compared to CCl_4 mice. Furthermore, we examined liver function by measuring alanine aminotransferase (ALT) levels in the plasma samples. Acute CCl_4 administration resulted in significantly increased plasma ALT levels (3.7-fold increase, $p < 0.001$) and ERA-SPIONs showed a significant decrease in plasma ALT levels (1.8-fold decrease, $p < 0.05$) compared to CCl_4 mice, which was not observed in free ERA-treated CCl_4 mice (Fig. 8C). Additionally, a single CCl_4 injection in mice led to a significant increase in collagen-I (2.7-fold increase, $p < 0.0001$) and α-SMA (5.6-fold increase, $p < 0.01$) protein expression compared to healthy mice (Fig. 8D and E). ERA-SPIONs significantly decreased collagen-I (1.6-fold decrease, $p < 0.001$) and α-SMA expression (3.3-fold decrease, $p < 0.05$) compared to CCl_4 mice and 1.5-fold and 1.8-fold decrease respectively compared to ERA-treated CCl_4 mice (Fig. 8D and E). Finally, we investigated the effects of ERA-SPIONs on gene expression of major fibrotic parameters and HSC activation markers *(Col1a1*, *Acta2*, *Timp1,* and *Pdgfrb)* in acute CCl_4-induced liver fibrosis (Fig. 8F). Acute CCl_4 administration caused upregulation of mRNA expression of *Col1a1*, *Acta2*, *Timp1,* and *Pdgfrb*. After treatment with ERA-SPIONs, a decreasing trend (modest inhibition) in *Col1a1*, *Acta2*, *Timp1,* and *Pdgfrb* expression was observed (Fig. 8F).

Since ETAR is specifically localized on HSCs (as also depicted in Fig. 1D), we do not expect any off-target effects of ERA-SPIONs on other liver cells. To rule out this possibility, we investigated the mRNA expression of genes *Cyp* (Cyp450), *Alb* (albumin), and *Ccnd1* (Cyclin D1) associated with hepatocytes functionality and viability, and *Adgre1* (F4/80) associated with the hepatic macrophages (Supplementary Fig. S18). No significant changes were observed in albumin, Cyp450, and F4/80

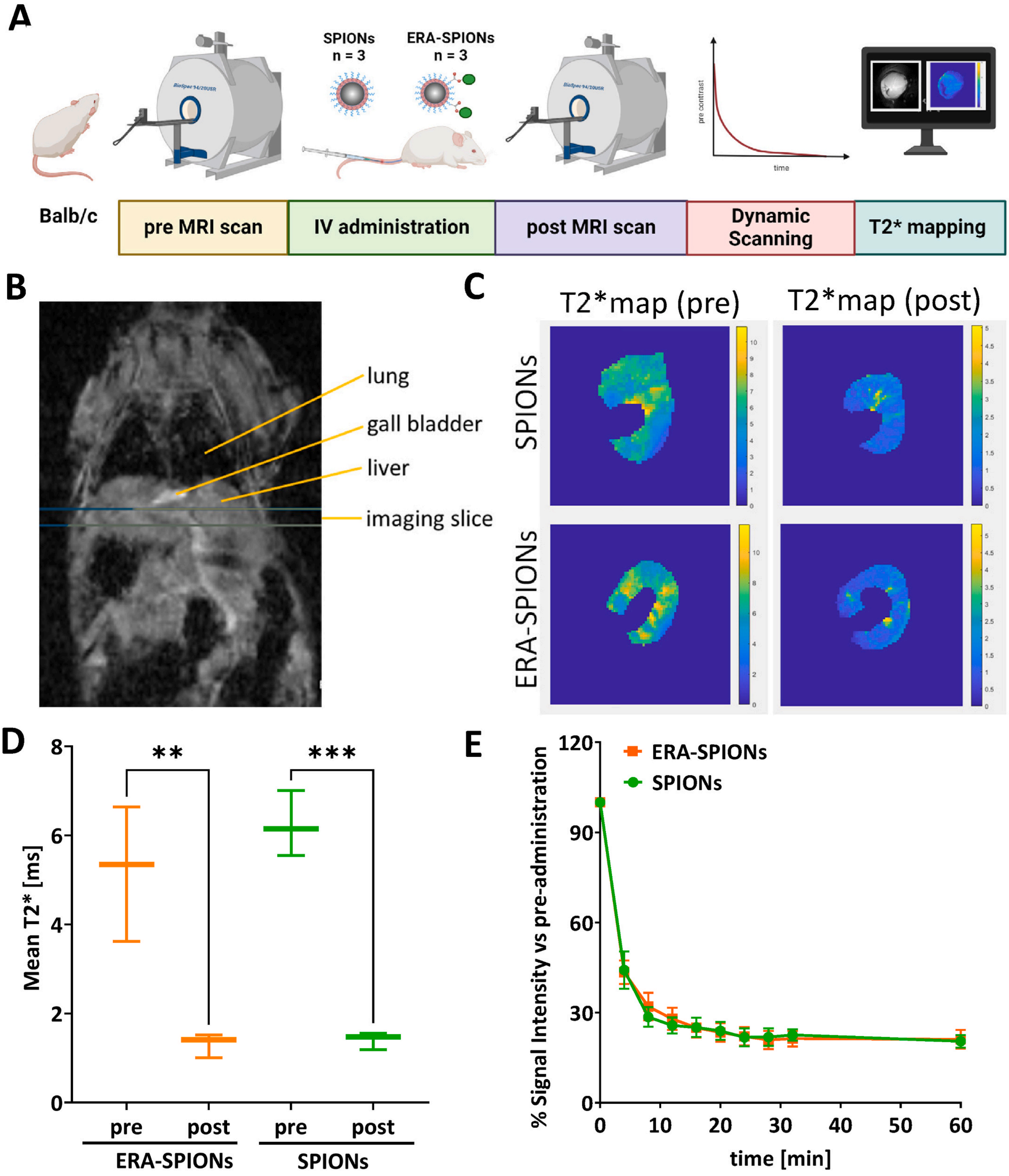

Fig. 6. In vivo MRI of SPIONs and ERA-SPIONs. (**A**) Schematic of the regimen of the in vivo MRI study and data analysis. (**B**) Representation of the abdominal region with organ positioning (lung, gall bladder, and liver) and the imaging slice for T2* mapping and dynamic scanning. **(C)** T2* maps retrieved from liver tissue pre and 30 min post administration of the SPIONs (150 μmol Fe/kg, n = 3) and ERA-SPIONs (150 μmol Fe/kg, n = 3). Complete set of images is provided in Supplementary Fig. S15. (**D**) A graph showing the mean and range of the quantified T2* (relaxation time) in ms pre and post administration of the SPIONs and ERA-SPIONs. (E) A graph showing % signal intensity versus pre-administration derived from the dynamic scanning analysis showing the accumulation of the SPIONs and ERA-SPIONs over time (min). Exemplary corresponding images are provided in Supplementary Fig. S16. The data are represented as mean ± SEM. Multiple comparisons between different groups (n = 5 per group) were performed by one-way analysis of variance (ANOVA) with a Bonferroni post hoc test. The differences were considered significant for a p-value of $^{**}p < 0.01$, $^{***}p < 0.001$.

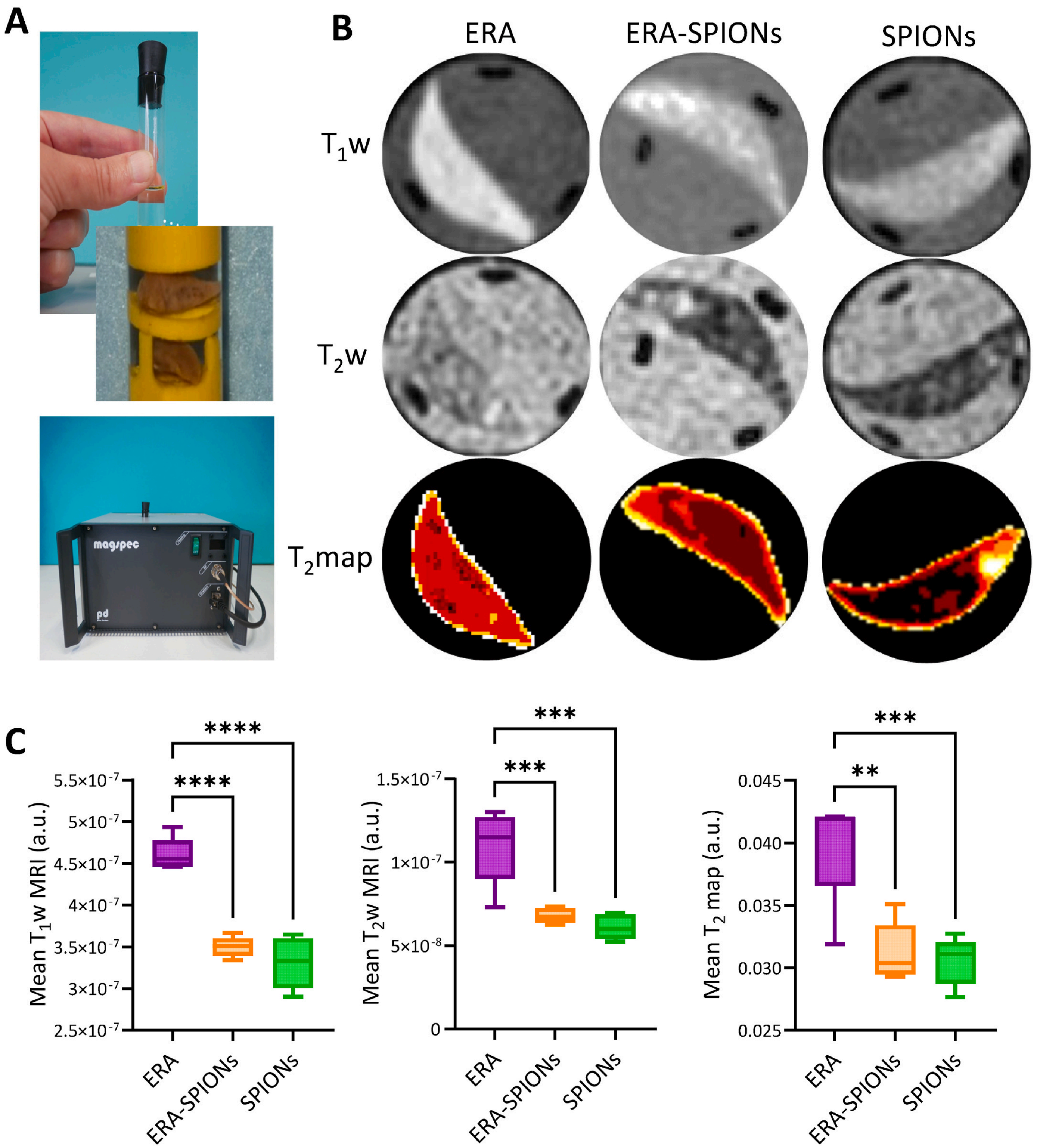

Fig. 7. Ex vivo MRI in ERA, ERA-SPIONs, and SPIONs in CCl_4-induced acute liver injury in mouse livers. (**A**) Photos showing a setup used for imaging of livers and a portable low-field MRI scanner system. (**B**) Representable images of T1-weighted (T_1w), T2-weighted (T_2w), T_2map images of livers. (**C**) Quantified T_1w, T_2w, and T_2map MRI sequences mean, median, and range. The data are represented as boxplots (2.5–97.5 percentile). Multiple comparisons between different groups (n = 5 per group) were performed by one-way analysis of variance (ANOVA) with a Bonferroni post hoc test. The differences were considered significant for a p-value of $^{**}p < 0.01$, $^{***}p < 0.001$, $^{****}p < 0.0001$.

expression levels suggesting that ERA and/or ERA-SPIONs have no effect on the hepatocyte functionality and hepatic macrophages. Cyclin D1 is a gatekeeper for the cell cycle, and the signaling pathways that trigger hepatocyte proliferation converge upon Cyclin D1. Impaired hepatocyte proliferation or hepatocyte damage represses Cyclin D1 as can be seen in CCl_4-mice compared to control healthy mice (1.9-fold decrease, $p < 0.01$), while ERA-SPIONs showed a modest (non-significant) increase in the Cyclin D1 (1.3-fold increase) indicating improved hepatocyte

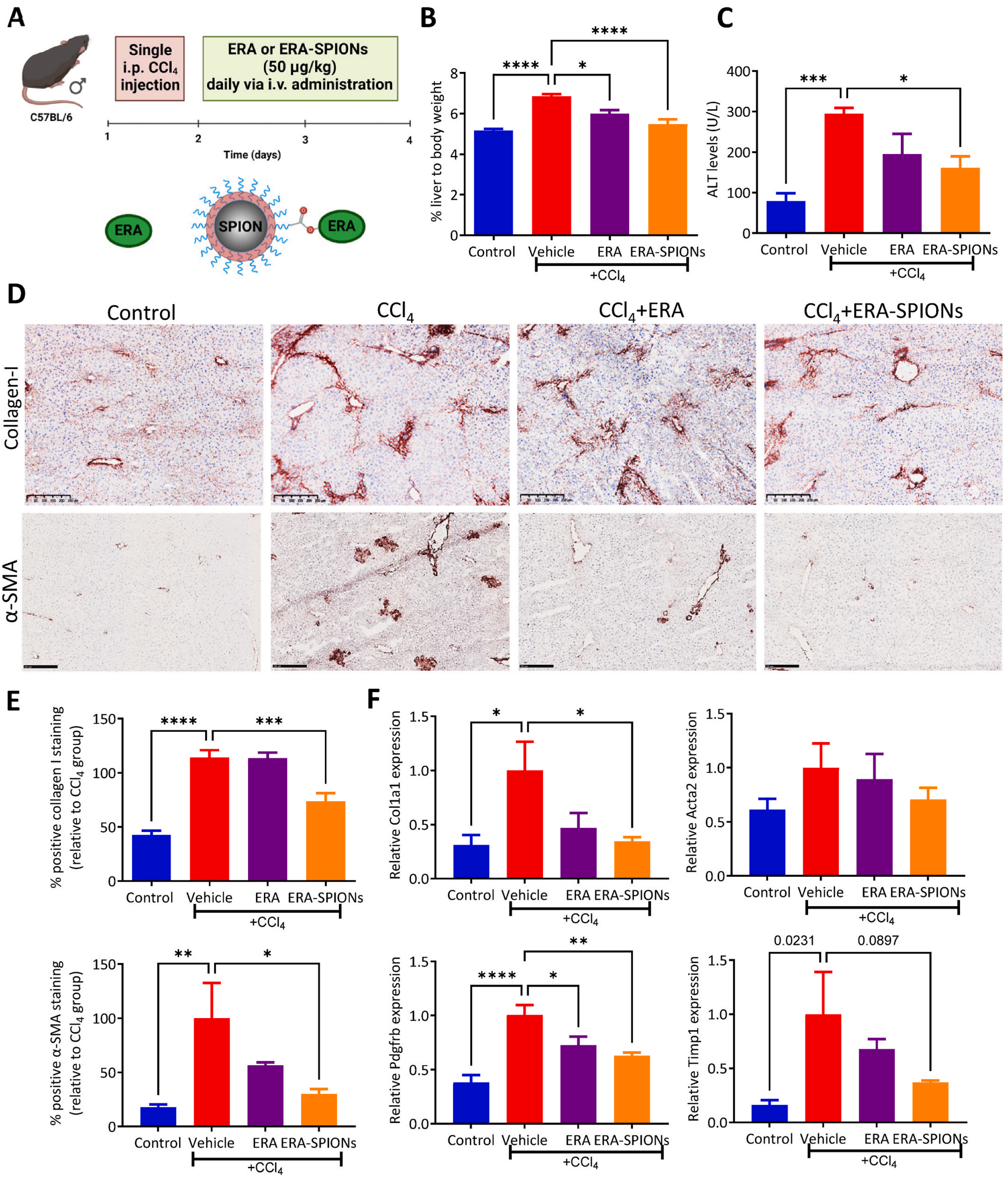

Fig. 8. Therapeutic effect of vehicle, ERA, and ERA-SPIONs in CCl_4-induced acute liver injury mouse model. (**A**) Schematic of the in vivo study and treatments. (**B**) Liver weights (respective to body weight) expressed in percentage. (**C**) Total alanine aminotransferase (ALT) plasma levels expressed in units (U)/L. (**D**) Representative images (scalebar = 250 μm) of immunohistochemical staining of collagen-I and α-SMA. (**E**) Quantified staining area of collagen-I and α-SMA IHC staining. (**F**) Relative mRNA expression (normalized to *Gapdh*) of *Col1a1*, *Acta2*, *Pdgfrb*, and *Timp1* (relative to vehicle control). The data are represented as mean + SEM. Multiple comparisons between different groups (n = 5 per group) were performed by one-way analysis of variance (ANOVA) with a Bonferroni post hoc test. The differences were considered significant for a p-value of $^*p < 0.05$, $^{**}p < 0.01$, $^{***}p < 0.001$, $^{****}p < 0.0001$.

regeneration/proliferation possibly due to HSC deactivation and/or decreased collagen deposition.

Altogether, these results indicate that ERA-SPIONs improved acute CCl_4-induced fibrotic liver injury in mice by inhibiting HSC activation.

4. Discussion

In this study, we present a novel theranostic nanomedicine approach aimed at improving the diagnosis and treatment of liver fibrosis by targeting endothelin A receptor antagonist (ETAR antagonist, ERA) using super-paramagnetic iron-oxide nanoparticles (SPIONs) to livers and more specifically to HSCs. We first confirmed the overexpression of endothelin-1 (ET-1) and ETAR in human cirrhotic livers, mouse fibrotic livers, and TGFβ-activated HSCs. Using single-cell Liver Cell Atlas, we observed that ETAR was specifically expressed on HSCs in both murine and human livers. Our in vitro studies demonstrated that ETAR antagonism using ERA and ERA-SPIONs effectively mitigated the TGFβ-induced activation of HSCs, inhibited ECM production, reduced contractility, and impeded cell migration. Additionally, in an in vivo CCl_4-induced acute liver fibrosis mouse model, ERA-SPIONs showed enhanced liver uptake and HSCs-specific localization resulting in reduced liver weight, improved liver function, and inhibited HSC activation and fibrosis (collagen deposition).

Hepatic fibrosis is a progressive pathological condition characterized by a prolonged wound-healing response, leading to the accumulation of ECM proteins, ultimately resulting in liver distortion and dysfunction [1–3]. Among various cell types involved, activated HSCs are the key pathogenic cells of fibrosis driving ECM production and deposition, making them a crucial therapeutic target for hepatic fibrosis treatment [4–8]. During liver injury, elevated levels of ET-1 are observed [20,21, 23–26], primarily activating HSCs via the endothelin pathway through ETAR [13,20,21,28]. In this study, we confirmed the upregulation of ET-1 and ETAR in human cirrhotic liver tissue, mouse fibrotic liver tissue, and TGFβ-activated HSCs. These results are consistent with the existing literature, where it has been described that TGFβ induces the expression and production of ET-1 in HSCs [23,27]. ET-1, in turn, promotes the activation of HSCs through ETAR, leading to further upregulation of ET-1 and ETAR expression, and stimulating the synthesis of ECM [26–29]. These findings support the role of the ET-1/ETAR pathway in the activation and fibrotic responses of HSCs. Subsequently, using the single-cell Liver Cell Atlas database [58], we substantiated that ETAR expression is specifically localized on the fibroblast/HSC subset of the liver cells in both humans and mice, making ETAR a promising therapeutic target for fibrosis.

Through the antagonism of the ET-1/ETAR pathway, it is possible to mitigate the activation, ECM production, contractility, and migration of HSCs [13,20]. In this study, we have demonstrated that ERA treatment dose-dependently attenuated the TGFβ-induced collagen-I and α-SMA expression at both gene and protein levels in HSCs. Furthermore, ERA dose-dependently ameliorated migration and contractility of TGFβ-activated HSCs. These findings suggest a significant attenuation of TGFβ-induced activation, ECM production, contractility, and migration upon treatment with ERA. Our results align with existing literature where, using in vivo models of hepatic fibrosis, it was shown that endothelin pathway antagonism led to reduced HSC activation and ECM production, ultimately resulting in reduced fibrosis [13,20,30–32].

The role of endothelin receptor antagonists has been investigated in the treatment of various diseases, including hypertension, diabetic nephropathy, pulmonary diseases, cardiovascular diseases, diabetes, and cancer [11–19]. For the treatment of pulmonary arterial hypertension, the FDA and EMA have approved endothelin antagonists such as Bosentan, Ambrisentan, and Macitentan [68]. Clinical trials using Bosentan (NCT00391443, NCT00071461), Ambrisentan (NCT00768300), and Macitentan (NCT00903331) in patients with pulmonary fibrosis yielded no significant effects [69–72]. These non-significant results can be attributed to the challenges associated with study design, patient selection, drug toxicity, and dosing, suggesting that successful trials utilizing endothelin receptor antagonists can be achieved with improved approaches [73]. Furthermore, the clinical potential of most endothelin antagonists is hindered due to the need for high/frequent dosing for therapeutic efficacy, resulting in a high incidence of side effects [74]. Most probably, it is due to the small size of these antagonists which often results in a short half-life (poor pharmacokinetics) and rapid clearance. In our study, we conjugated ERA to SPIONs to improve pharmacokinetics and enhance hepatic uptake, thus enabling reduced frequency of high dosing, minimizing systemic side effects, and maximizing therapeutic efficacy.

To enhance the pharmacokinetics of small molecules, various types of nanocarriers have been developed [35–37]. These nanocarriers can be used as carriers for the delivery of drugs to the liver for the treatment of liver fibrosis and/or for the delivery of contrast agents for the diagnosis/staging of liver fibrosis. The criteria for selecting the nanocarrier in this study included a spherical shape, a size range between 10 and 150 nm, a negative surface charge, and surface modification including PEG-coating and ERA-conjugation [75]. Compared to other nanocarriers, SPIONs fulfill all the desired criteria, are FDA-approved, and offer several advantages, including small size, dextran-PEG coating, large surface area, ease of ligand/drug conjugation, and detectability through MRI [38–41]. SPIONs can be used both for therapy and diagnosis (theranostic) of liver fibrosis [76]. It has to be noted that the size and surface properties of SPIONs can influence the liver and cellular uptake, cytotoxicity, distribution, and clearance of SPIONs [77]. Notably, SPIONs are shown to be not toxic to the liver cells and do not affect the liver function in different animal models [78]. In this study, we used SPIONs for conjugating ERA which were used in our previous studies [42–45].

It is important to consider that the conjugation of nanoparticles can potentially diminish the activity of the antagonist due to the blocking of the interaction site or steric hindrance. To address this concern, Höltke et al. successfully modified PD-156707, a selective endothelin A receptor antagonist [51,52], by incorporating a PEG-spacer containing an amino moiety (CH948; ERA). This specific alteration allows for the conjugation of ERA with other molecules while preserving its biological activity [54]. Our in vitro studies confirmed that ERA-SPIONs retained their biological activity, as evidenced by their binding capacity to activated HSCs, and inhibition of HSC activation, proliferation, migration, and ECM production. Interestingly, ERA-SPIONs showed superior inhibitory effects compared to free ERA. This may possibly be attributed to the PEG-spacer of ERA that might decrease the affinity to ERA, while multivalent interaction, facilitated by conjugation to the SPIONs, counterbalances the affinity loss by increased avidity that immensely increases the interaction between antagonist and receptor [79].

In our study, we examined the hepatic uptake of free ERA, a small molecule with limited hepatic uptake, and investigated whether conjugation to SPIONs could enhance its hepatic uptake. To assess this, we performed a biodistribution study in an acute CCl_4-induced liver fibrosis mouse model using Cy5.5-conjugated ERA and ERA-SPIONs. The results demonstrated that ERA-SPIONs exhibited higher liver uptake compared to free ERA. This is in accordance with our previous studies [42,45] and with the literature, where Keselman et al. showed that SPIONs were cleared out of the blood within hours, however, enhanced SPION activity in the liver was observed for multiple days [80]. The increased hepatic uptake of ERA is most likely due to the passive liver uptake of SPIONs owing to the physicochemical properties of the nanoparticles, due to the rich vasculature and unique metabolic capacity of the liver [8, 81–83]. This enhanced liver uptake of ERA-SPIONs suggests the potential of utilizing SPIONs as a strategy to improve the liver delivery of ERA for therapeutic applications. Additionally, ERA-SPIONs were co-localized with the HSCs within the liver, suggesting HSCs-selective binding of ERA-SPIONs and HSCs-selective ETAR antagonism. Subsequently, we assessed the anti-fibrotic effects of ERA and ERA-SPIONs in an acute CCl_4-induced liver fibrosis mouse model. Upon administration of ERA-SPIONs, a significant reduction in liver weight, improvement in liver function tests (ALT levels), and collagen-I (and α-SMA expression) were observed, indicating significant anti-fibrotic activity. Conversely, the administration of ERA alone, although showing a decreasing trend, did not lead to a significant decrease in these fibrotic markers. These findings collectively suggest that conjugation of ERA to SPIONs enhances the half-life, avidity, and liver accumulation of ERA and HSC-specific localization of SPIONs. Consequently, this improvement contributes to an enhanced therapeutic efficacy of ERA-SPIONs in vivo. These results strongly support the notion that the conjugation of ERA to SPIONs serves as a promising strategy to optimize the therapeutic outcomes of ERA in the treatment of fibrosis.

The utilization of SPIONs as carriers for ERA allows for the dual functionality i.e., targeted therapy and MRI-based imaging. The in vivo and ex vivo MRI results showed that the presence of ERA-SPIONs in the liver tissues resulted in low-intensity signals in MRI images and reduced T2 and T2* values, indicating the successful detection of the nanoparticles in the affected tissues. We have previously emphasized on the utility of SPIONs as a diagnostic tool via MRI detection and demonstrated the diagnostic properties of SPIONs in a CCl_4-induced liver cirrhosis mouse model [45]. By exploring the imaging capabilities of MRI in detecting ERA-SPIONs in liver tissues, our study contributes to the development of an advanced theranostic nanomedicine platform for liver fibrosis. This may pave the way for future studies investigating the full potential of multimodal imaging and targeted therapeutic approaches in liver fibrosis management and other fibrotic diseases.

When considering SPIONs for clinical application, it is important to understand the fate of these particles in the body. Previously, Ashraf et al. [84] studied the in vivo fate of free and encapsulated (in capsules) SPIONs and found that both free and encapsulated SPIONs were enriched in the liver and were not completely eliminated 2 weeks post-injection suggesting longer circulation and liver retention of SPIONs [84]. Kolosnjaj-Tabi et al. analyzed the long-term (one-year) fate of iron oxide-coated gold nanoparticles in mice, and demonstrated a progressive decrease in quantities of magnetic iron oxide over time (faster for PEG-coated compared to polymer-coated), which is attributed to the dissolution rather than excretion of intact particles [85]. One hypothesis proposed is the local transfer of released iron to proximal ferritin proteins, as suggested by TEM observations. We expect that ERA-SPIONs enriched in the liver will be gradually degraded in the liver, releasing different nanoparticle components over time which will be transferred to proximal proteins and removed via excretion mechanisms. However, more studies are needed in this direction.

To the best of our knowledge, this study represents the first investigation of the therapeutic effects of nanoparticle-mediated endothelin antagonism in hepatic fibrosis, addressing the challenge of side effects associated with traditional approaches. However, it is important to acknowledge that the in vivo model utilized in our study represents early-stage liver fibrosis and may not fully replicate the complexity of the clinical situation. Nonetheless, our findings strongly support the potential therapeutic application of ERA-SPIONs as a promising approach for targeting liver fibrosis. Future studies are needed, so we can advance the development and optimization of ERA-SPIONs as a potential therapeutic strategy for various fibrotic conditions.

5. Conclusion

Our study provides compelling evidence supporting the potential of utilizing SPIONs for the delivery of ERA as a promising therapeutic strategy for liver fibrosis. Our findings demonstrate that this approach enhances the therapeutic efficacy of ERA both in in vitro and in vivo settings. Moreover, the utilization of SPIONs allows for MRI-based diagnosis, enabling a personalized theranostic approach that combines therapy and diagnosis for tailored disease management. Altogether, this study presents a novel approach for the delivery of ERA for an effective treatment of liver fibrosis.

Ethics approval and consent to participate

All animal experiments were performed in strict accordance with the guidelines and regulations for the Care and Use of Laboratory Animals. The study protocols were approved by the Institutional Animal Ethics Committee of the University of Twente, Enschede, The Netherlands or the University Hospital Muenster, Muenster, Germany.

CRediT authorship contribution statement

Marit ten Hove: Writing – original draft, Writing – review & editing, Methodology, Investigation, Formal analysis, Data curation. **Andreas Smyris:** Methodology, Investigation, Data curation. **Richell Booijink:** Methodology, Investigation, Formal analysis, Data curation. **Lydia Wachsmuth:** Writing – review & editing, Methodology, Investigation, Formal analysis. **Uwe Hansen:** Methodology, Data curation. **Lejla Alic:** Writing – original draft, Methodology, Investigation, Formal analysis, Data curation. **Cornelius Faber:** Writing – review & editing, Resources. **Carsten Höltke:** Writing – review & editing, Supervision, Funding acquisition, Formal analysis, Data curation. **Ruchi Bansal:** Writing – review & editing, Supervision, Resources, Project administration, Funding acquisition, Formal analysis, Data curation, Conceptualization.

Declaration of competing interest

The authors declare that they have no known competing financial interests or personal relationships that could have appeared to influence the work reported in this paper.

Acknowledgements

This work was supported by the UT-WWU Booster grant created to stimulate Cross-border Collaboration UT Twente-WWU Muenster On Imaging for Diagnosis and Therapy funded to Ruchi Bansal and Carsten Höltke. We acknowledge the Twente Graduate School at the University of Twente for providing the TGS bridging grant to Marit ten Hove for finalizing this study. We also acknowledge the support of Martina Tsvetanova and Mark Smithers (University of Twente, Netherlands) for performing the SEM, TEM and EDX measurements, Dr. Gerald Kehr and Kathrin Bussmann (University Hospital Muenster, Germany) for their help with the FTIR measurements, and Peng Liu (University of Twente, Netherlands) for his help with the VSM measurements.

Appendix A. Supplementary data

Supplementary data to this article can be found online at https://doi.org/10.1016/j.bioactmat.2024.05.034.

References

[1] S.L. Friedman, Hepatic fibrosis – overview, Toxicology 254 (3) (2008) 120–129.

[2] R. Bataller, D.A. Brenner, Liver fibrosis, J. Clin. Invest. 115 (2) (2005) 209–218.

[3] R. Bansal, B. Nagorniewicz, J. Prakash, Clinical advancements in the targeted therapies against liver fibrosis, Mediat. Inflamm. 2016 (2016) 7629724.

[4] S.L. Friedman, Hepatic stellate cells: protean, multifunctional, and enigmatic cells of the liver, Physiol. Rev. 88 (1) (2008) 125–172.

[5] T. Higashi, S.L. Friedman, Y. Hoshida, Hepatic stellate cells as key target in liver fibrosis, Adv. Drug Deliv. Rev. 121 (2017) 27–42.

[6] D. Li, S.L. Friedman, Liver fibrogenesis and the role of hepatic stellate cells: new insights and prospects for therapy, J. Gastroenterol. Hepatol. 14 (7) (1999) 618–633.

[7] S. Yazdani, R. Bansal, J. Prakash, Drug targeting to myofibroblasts: implications for fibrosis and cancer, Adv. Drug Deliv. Rev. 121 (2017) 101–116.

[8] R. Bansal, K. Poelstra, Hepatic stellate cell targeting using peptide-modified biologicals, Methods Mol. Biol. 2669 (2023) 269–284.

[9] C. Trautwein, S.L. Friedman, D. Schuppan, M. Pinzani, Hepatic fibrosis: concept to treatment, J. Hepatol. 62 (1 Suppl) (2015) S15–S24.

[10] K. Poelstra, Liver fibrosis in 2015: crucial steps towards an effective treatment, Nat. Rev. Gastroenterol. Hepatol. 13 (2) (2016) 67–68.

[11] M. Yanagisawa, H. Kurihara, S. Kimura, Y. Tomobe, M. Kobayashi, Y. Mitsui, et al., A novel potent vasoconstrictor peptide produced by vascular endothelial cells, Nature 332 (6163) (1988) 411–415.

[12] F. Bohm, J. Pernow, The importance of endothelin-1 for vascular dysfunction in cardiovascular disease, Cardiovasc. Res. 76 (1) (2007) 8–18.

[13] D.C. Rockey, J.J. Chung, Endothelin antagonism in experimental hepatic fibrosis. Implications for endothelin in the pathogenesis of wound healing, J. Clin. Invest. 98 (6) (1996) 1381–1388.

[14] K. Banecki, K.A. Dora, Endothelin-1 in health and disease, Int. J. Mol. Sci. 24 (14) (2023).

[15] V. Gulberg, A.L. Gerbes, Relation of endothelins to volume regulating neurohumoral systems in patients with cirrhosis of the liver, Eur. J. Clin. Invest. 25 (12) (1995) 893–898.

[16] W. Yuan, Y. Li, J. Wang, J. Li, S. Gou, P. Fu, Endothelin-receptor antagonists for diabetic nephropathy: a meta-analysis, Nephrology 20 (7) (2015) 459–466.

[17] M. Barton, M. Yanagisawa, Endothelin: 30 Years from discovery to therapy, Hypertension 74 (6) (2019) 1232–1265.

[18] A. Jain, C. Coffey, V. Mehrotra, J. Flammer, Endothelin-1 traps as a potential therapeutic tool: from diabetes to beyond? Drug Discov. Today 24 (9) (2019) 1937–1942.

[19] L. Rosano, A. Bagnato, Endothelin therapeutics in cancer: where are we? Am. J. Physiol. Regul. Integr. Comp. Physiol. 310 (6) (2016) R469–R475.

[20] D.C. Rockey, R.A. Weisiger, Endothelin induced contractility of stellate cells from normal and cirrhotic rat liver: implications for regulation of portal pressure and resistance, Hepatology 24 (1) (1996) 233–240.

[21] D.C. Rockey, Characterization of endothelin receptors mediating rat hepatic stellate cell contraction, Biochem. Biophys. Res. Commun. 207 (2) (1995) 725–731.

[22] L. Rosano, F. Spinella, A. Bagnato, Endothelin 1 in cancer: biological implications and therapeutic opportunities, Nat. Rev. Cancer 13 (9) (2013) 637–651.

[23] B. Degertekin, S. Ozenirler, S. Elbeg, G. Akyol, The serum endothelin-1 level in steatosis and NASH, and its relation with severity of liver fibrosis, Dig. Dis. Sci. 52 (10) (2007) 2622–2628.

[24] H. Kong, J. He, S. Guo, Q. Song, D. Xiang, R. Tao, et al., Endothelin receptors promote schistosomiasis-induced hepatic fibrosis via splenic B cells, PLoS Pathog. 16 (10) (2020) e1008947.

[25] P.W. Angus, Role of endothelin in systemic and portal resistance in cirrhosis, Gut 55 (9) (2006) 1230–1232.

[26] M. Pinzani, S. Milani, R. De Franco, C. Grappone, A. Caligiuri, A. Gentilini, et al., Endothelin 1 is overexpressed in human cirrhotic liver and exerts multiple effects on activated hepatic stellate cells, Gastroenterology 110 (2) (1996) 534–548.

[27] M. Clozel, H. Salloukh, Role of endothelin in fibrosis and anti-fibrotic potential of bosentan, Ann. Med. 37 (1) (2005) 2–12.

[28] S. Takashimizu, S. Kojima, Y. Nishizaki, T. Kagawa, K. Shiraishi, T. Mine, et al., Effect of endothelin A receptor antagonist on hepatic hemodynamics in cirrhotic rats. Implications for endothelin-1 in portal hypertension, Tokai J. Exp. Clin. Med. 36 (2) (2011) 37–43.

[29] D.C. Rockey, Vasoactive agents in intrahepatic portal hypertension and fibrogenesis: implications for therapy, Gastroenterology 118 (6) (2000) 1261–1265.

[30] C. Thirunavukkarasu, Y. Yang, V.M. Subbotin, S.A. Harvey, J. Fung, C.R. Gandhi, Endothelin receptor antagonist TAK-044 arrests and reverses the development of carbon tetrachloride induced cirrhosis in rats, Gut 53 (7) (2004) 1010–1019.

[31] H.Q. Feng, N.D. Weymouth, D.C. Rockey, Endothelin antagonism in portal hypertensive mice: implications for endothelin receptor-specific signaling in liver disease, Am. J. Physiol. Gastrointest. Liver Physiol. 297 (1) (2009) G27–G33.

[32] J.J. Cho, B. Hocher, H. Herbst, J.D. Jia, M. Ruehl, E.G. Hahn, et al., An oral endothelin-A receptor antagonist blocks collagen synthesis and deposition in advanced rat liver fibrosis, Gastroenterology 118 (6) (2000) 1169–1178.

[33] T. Fukuroda, T. Fujikawa, S. Ozaki, K. Ishikawa, M. Yano, M. Nishikibe, Clearance of circulating endothelin-1 by ETB receptors in rats, Biochem. Biophys. Res. Commun. 199 (3) (1994) 1461–1465.

[34] S. Motte, K. McEntee, R. Naeije, Endothelin receptor antagonists, Pharmacol. Therapeut. 110 (3) (2006) 386–414.

[35] D. Peer, J.M. Karp, S. Hong, O.C. Farokhzad, R. Margalit, R. Langer, Nanocarriers as an emerging platform for cancer therapy, Nat. Nanotechnol. 2 (12) (2007) 751–760.

[36] O.C. Farokhzad, R. Langer, Nanomedicine: developing smarter therapeutic and diagnostic modalities, Adv. Drug Deliv. Rev. 58 (14) (2006) 1456–1459.

[37] S. Hassan, G. Prakash, A. Ozturk, S. Saghazadeh, M.F. Sohail, J. Seo, et al., Evolution and clinical translation of drug delivery nanomaterials, Nano Today 15 (2017) 91–106.

[38] C. Tassa, S.Y. Shaw, R. Weissleder, Dextran-coated iron oxide nanoparticles: a versatile platform for targeted molecular imaging, molecular diagnostics, and therapy, Acc. Chem. Res. 44 (10) (2011) 842–852.

[39] F. Dilnawaz, A. Singh, C. Mohanty, S.K. Sahoo, Dual drug loaded superparamagnetic iron oxide nanoparticles for targeted cancer therapy, Biomaterials 31 (13) (2010) 3694–3706.

[40] J.E. Rosen, L. Chan, D.B. Shieh, F.X. Gu, Iron oxide nanoparticles for targeted cancer imaging and diagnostics, Nanomedicine 8 (3) (2012) 275–290.

[41] M. Arruebo, R. Fernández-Pacheco, M.R. Ibarra, J. Santamaría, Magnetic nanoparticles for drug delivery, Nano Today 2 (3) (2007) 22–32.

[42] D.W. Kurniawan, R. Booijink, L. Pater, I. Wols, A. Vrynas, G. Storm, et al., Fibroblast growth factor 2 conjugated superparamagnetic iron oxide nanoparticles (FGF2-SPIONs) ameliorate hepatic stellate cells activation in vitro and acute liver injury in vivo, J. Contr. Release 328 (2020) 640–652.

[43] D.F. Mardhian, G. Storm, R. Bansal, J. Prakash, Nano-targeted relaxin impairs fibrosis and tumor growth in pancreatic cancer and improves the efficacy of gemcitabine in vivo, J. Contr. Release 290 (2018) 1–10.

[44] D.F. Mardhian, A. Vrynas, G. Storm, R. Bansal, J. Prakash, FGF2 engineered SPIONs attenuate tumor stroma and potentiate the effect of chemotherapy in 3D heterospheroidal model of pancreatic tumor, Nanotheranostics 4 (1) (2020) 26–39.

[45] B. Nagorniewicz, D.F. Mardhian, R. Booijink, G. Storm, J. Prakash, R. Bansal, Engineered Relaxin as theranostic nanomedicine to diagnose and ameliorate liver cirrhosis, Nanomedicine 17 (2019) 106–118.

[46] T. Huang, T. Zhang, X. Jiang, A. Li, Y. Su, Q. Bian, et al., Iron oxide nanoparticles augment the intercellular mitochondrial transfer-mediated therapy, Sci. Adv. 7 (40) (2021) eabj0534.

[47] L. Zheng, Z. Zhuang, Y. Li, T. Shi, K. Fu, W. Yan, et al., Bone targeting antioxidative nano-iron oxide for treating postmenopausal osteoporosis, Bioact. Mater. 14 (2022) 250–261.

[48] Z. Lv, P. Wang, W. Li, Y. Xie, W. Sun, X. Jin, et al., Bifunctional TRPV1 targeted magnetothermal switch to attenuate osteoarthritis progression, Research 7 (2024) 316.

[49] E. Hoffmann, M. Masthoff, W.G. Kunz, M. Seidensticker, S. Bobe, M. Gerwing, et al., Multiparametric MRI for characterization of the tumour microenvironment, Nat. Rev. Clin. Oncol. 21 (2024) 428–448.

[50] D. Lau, P.G. Corrie, F.A. Gallagher, MRI techniques for immunotherapy monitoring, J Immunother Cancer 10 (9) (2022).

[51] A.M. Doherty, W.C. Patt, J.J. Edmunds, K.A. Berryman, B.R. Reisdorph, M. S. Plummer, et al., Discovery of a novel series of orally active non-peptide endothelin-A (ETA) receptor-selective antagonists, J. Med. Chem. 38 (8) (1995) 1259–1263.

[52] A.M. Doherty, A.C. Uprichard, Discovery and development of an endothelin A receptor-selective antagonist PD 156707, Pharmaceut. Biotechnol. 11 (1998) 81–112.

[53] C. Holtke, A. von Wallbrunn, K. Kopka, O. Schober, W. Heindel, M. Schafers, et al., A fluorescent photoprobe for the imaging of endothelin receptors, Bioconjugate Chem. 18 (3) (2007) 685–694.

[54] C. Holtke, M.P. Law, S. Wagner, H.J. Breyholz, K. Kopka, C. Bremer, et al., Synthesis, in vitro pharmacology and biodistribution studies of new PD 156707-derived ET(A) receptor radioligands, Bioorg. Med. Chem. 14 (6) (2006) 1910–1917.

[55] K. Buther, M.G. Compeer, J.G. De Mey, O. Schober, M. Schafers, C. Bremer, et al., Assessment of endothelin-A receptor expression in subcutaneous and orthotopic thyroid carcinoma xenografts in vivo employing optical imaging methods, Endocrinology 153 (6) (2012) 2907–2918.

[56] M.A. Kimm, H. Haas, M. Stolting, M. Kuhlmann, C. Geyer, S. Glasl, et al., Targeting endothelin receptors in a murine model of myocardial infarction using a small molecular fluorescent probe, Mol. Pharm. 17 (1) (2020) 109–117.

[57] V.R. Mas, D.G. Maluf, K.J. Archer, K. Yanek, X. Kong, L. Kulik, et al., Genes involved in viral carcinogenesis and tumor initiation in hepatitis C virus-induced hepatocellular carcinoma, Mol. Med. 15 (3–4) (2009) 85–94.

[58] M. Guilliams, J. Bonnardel, B. Haest, B. Vanderborght, C. Wagner, A. Remmerie, et al., Spatial proteogenomics reveals distinct and evolutionarily conserved hepatic macrophage niches, Cell 185 (2) (2022) 379–396 e38.

[59] E.E. Reynolds, J.A. Keiser, S.J. Haleen, D.M. Walker, B. Olszewski, R.L. Schroeder, et al., Pharmacological characterization of PD 156707, an orally active ETA receptor antagonist, J. Pharmacol. Exp. Therapeut. 273 (3) (1995) 1410–1417.

[60] A. Ozdemir, M.S. Ekiz, A. Dilli, M.O. Guler, A.B. Tekinay, Amphiphilic peptide coated superparamagnetic iron oxide nanoparticles for in vivo MR tumor imaging, RSC Adv. 6 (51) (2016) 45135–45146.

[61] W. Tanaka, N. Yamanaka, M. Onishi, M. Ko, J. Yamanaka, E. Okamoto, Optimal route of administration of mixed endothelin receptor antagonist (TAK-044) in liver transplantation, J. Gastroenterol. 35 (2) (2000) 120–126.

[62] M. Kavanagh, B. Battistini, S. Jean, J. Crochetiere, L. Fournier, J. Wessale, et al., Effect of ABT-627 (A-147627), a potent selective ET(A) receptor antagonist, on the cardiopulmonary profile of newborn lambs with surgically-induced diaphragmatic hernia, Br. J. Pharmacol. 134 (8) (2001) 1679–1688.

[63] Arthur de Lange, Lejla Alić, Haken Bt, F.F.J. Simonis, Accelerated imaging of resected lymph nodes at high spatial resolution using a portable low-field MRI scanner. Joint Annual Meeting ISMRM–ISMRT, 2023, p. 2023.

[64] J. Anderson, T2 Mapping Compared to Standard MRI Assessment, KTH Royal Institute of Technology, Stockholm, 2018.

[65] T. Emrich, F. Hahn, D. Fleischmann, M.C. Halfmann, C. Duber, A. Varga-Szemes, et al., T1 and T2 mapping to detect chronic inflammation in cardiac magnetic resonance imaging in heart failure with reduced ejection fraction, ESC Heart Fail 7 (5) (2020) 2544–2552.

[66] M. Schacht, D. Mohammadi, N. Schützenmeister, Pd-Catalyzed synthesis of γ-keto esters as key intermediates for the synthesis of γ-hydroxybutenolides, Eur. J. Org Chem. 2019 (15) (2019) 2587–2591.

[67] M. Rohrer, H. Bauer, J. Mintorovitch, M. Requardt, H.J. Weinmann, Comparison of magnetic properties of MRI contrast media solutions at different magnetic field strengths, Invest. Radiol. 40 (11) (2005) 715–724.

[68] F.C. Enevoldsen, J. Sahana, M. Wehland, D. Grimm, M. Infanger, M. Kruger, Endothelin receptor antagonists: status quo and future perspectives for targeted therapy, J. Clin. Med. 9 (3) (2020).

[69] G. Raghu, R. Million-Rousseau, A. Morganti, L. Perchenet, J. Behr, Macitentan for the treatment of idiopathic pulmonary fibrosis: the randomised controlled MUSIC trial, Eur. Respir. J. 42 (6) (2013) 1622–1632.

[70] G. Raghu, J. Behr, K.K. Brown, J.J. Egan, S.M. Kawut, K.R. Flaherty, et al., Treatment of idiopathic pulmonary fibrosis with ambrisentan: a parallel, randomized trial, Ann. Intern. Med. 158 (9) (2013) 641–649.

[71] T.E. King Jr., J. Behr, K.K. Brown, R.M. du Bois, L. Lancaster, J.A. de Andrade, et al., BUILD-1: a randomized placebo-controlled trial of bosentan in idiopathic pulmonary fibrosis, Am. J. Respir. Crit. Care Med. 177 (1) (2008) 75–81.

[72] T.E. King Jr., K.K. Brown, G. Raghu, R.M. du Bois, D.A. Lynch, F. Martinez, et al., BUILD-3: a randomized, controlled trial of bosentan in idiopathic pulmonary fibrosis, Am. J. Respir. Crit. Care Med. 184 (1) (2011) 92–99.

[73] D.E. Kohan, J.G. Cleland, L.J. Rubin, D. Theodorescu, M. Barton, Clinical trials with endothelin receptor antagonists: what went wrong and where can we improve? Life Sci. 91 (13–14) (2012) 528–539.

[74] I. Lazich, G.L. Bakris, Endothelin antagonism in patients with resistant hypertension and hypertension nephropathy, Contrib. Nephrol. 172 (2011) 223–234.

[75] N. Hoshyar, S. Gray, H. Han, G. Bao, The effect of nanoparticle size on in vivo pharmacokinetics and cellular interaction, Nanomedicine 11 (6) (2016) 673–692.

[76] A. Neuwelt, N. Sidhu, C.A. Hu, G. Mlady, S.C. Eberhardt, L.O. Sillerud, Iron-based superparamagnetic nanoparticle contrast agents for MRI of infection and inflammation, AJR Am. J. Roentgenol. 204 (3) (2015) W302–W313.

[77] Q. Feng, Y. Liu, J. Huang, K. Chen, J. Huang, K. Xiao, Uptake, distribution, clearance, and toxicity of iron oxide nanoparticles with different sizes and coatings, Sci. Rep. 8 (1) (2018) 2082.

[78] R. Vakili-Ghartavol, A.A. Momtazi-Borojeni, Z. Vakili-Ghartavol, H.T. Aiyelabegan, M.R. Jaafari, S.M. Rezayat, et al., Toxicity assessment of superparamagnetic iron oxide nanoparticles in different tissues, Artif. Cells, Nanomed. Biotechnol. 48 (1) (2020) 443–451.

[79] R. Hennig, K. Pollinger, A. Veser, M. Breunig, A. Goepferich, Nanoparticle multivalency counterbalances the ligand affinity loss upon PEGylation, J. Contr. Release 194 (2014) 20–27.

[80] P. Keselman, E.Y. Yu, X.Y. Zhou, P.W. Goodwill, P. Chandrasekharan, R. M. Ferguson, et al., Tracking short-term biodistribution and long-term clearance of SPIO tracers in magnetic particle imaging, Phys. Med. Biol. 62 (9) (2017) 3440–3453.

[81] H. Wang, C.A. Thorling, X. Liang, K.R. Bridle, J.E. Grice, Y. Zhu, et al., Diagnostic imaging and therapeutic application of nanoparticles targeting the liver, J. Mater. Chem. B 3 (6) (2015) 939–958.

[82] F. Athanasopoulou, M. Manolakakis, S. Vernia, N. Kamaly, Nanodrug delivery systems for metabolic chronic liver diseases: advances and perspectives, Nanomedicine 18 (1) (2023) 67–84.

[83] L.H. Reddy, P. Couvreur, Nanotechnology for therapy and imaging of liver diseases, J. Hepatol. 55 (6) (2011) 1461–1466.

[84] S. Ashraf, A. Taylor, J. Sharkey, M. Barrow, P. Murray, B. Wilm, et al., In vivo fate of free and encapsulated iron oxide nanoparticles after injection of labelled stem cells, Nanoscale Adv. 1 (1) (2019) 367–377.

[85] J. Kolosnjaj-Tabi, Y. Javed, L. Lartigue, J. Volatron, D. Elgrabli, I. Marangon, et al., The one year fate of iron oxide coated gold nanoparticles in mice, ACS Nano 9 (8) (2015) 7925–7939.